Atomic Energy Control Board
P.O. Box 1046
Ottawa, Canada
K1P 5S9

Commission de contrôle de l'énergie atomique
C.P. 1046
Ottawa, Canada
K1P 5S9

INFO-0188

GAS AND WATER PERMEABILITY OF CONCRETE FOR REACTOR BUILDINGS -- SMALL SPECIMENS

by

R.H. Mills
University of Toronto

A research report prepared for the
Atomic Energy Control Board
Ottawa, Canada

March 1986

Canada

Research report

86-05422/

GAS AND WATER PERMEABILITY OF CONCRETE FOR REACTOR BUILDINGS -- SMALL SPECIMENS

ABSTRACT

The effect on permeability of artificial aging by drying shrinkage and by freeze-thaw was determined by observing mass transfer of gas and water under a pressure gradient. It was found that damage due to freeze-thaw was negligible but that cracking around aggregate caused by drying shrinkage resulted in significantly increased permeability to both gas and water. The absence of freeze-thaw damage was attributed to self-dessication. Since the concrete was not exposed to an external source of water, the chemical reaction was sustained by consumption of mixing water. The resulting air voids were, apparently, sufficient to absorb expansive pressures due to ice formation.

The response to lateral prestress was different for cracked and uncracked concrete. Although, in all cases, increased prestress resulted in reduced leakage, the effect was stronger in cracked concrete. Mean pore diameter as determined by gas diffusion was not, however, substantially affected because the leakage in cracked concrete remained very low.

Reinforcing steel did not have a great influence on permeability of small specimens.

Gas transmission through concrete was strongly influenced by moisture content. Free moisture constituted a barrier to gas flow, acting as a virtual solid. This is important since aging of concrete results in reduced free moisture.

Ultrasonic pulse velocity appeared to vary with moisture content and porosity of concrete in the same way as gas permeability and gave promise of being effective for in-situ monitoring of concrete in reactor buildings.

DISCLAIMER

The Atomic Energy Control Board is not responsible for the accuracy of the statements made or opinions expressed in this publication and neither the Board nor the author assumes liability with respect to any damage or loss incurred as a result of the use made of the information contained in this publication.

PERMÉABILITÉ AU GAZ ET À L'EAU DU BÉTON DES ENCEINTES DE CONFINEMENT DES RÉACTEURS -- PETITS SPÉCIMENS

RÉSUMÉ

L'observation du transfert de masse du gaz et de l'eau sous un gradient de pression a permis de déterminer l'effet sur la perméabilité du vieillissement artificiel du béton créé par la contraction par séchage et par le processus gel-dégel. Il a été constaté que le dommage dû au processus gel-dégel était négligeable, mais que les fractures autour des agrégats causées par la contraction par séchage ont provoqué un accroissement de la perméabilité au gaz et à l'eau. L'absence de dommage dû au processus gel-dégel a été attribuée à l'auto-dessication. Parce que le béton n'était pas exposé à une source d'eau externe, la réaction chimique a été entretenue par la consommation de l'eau du gâchage. Les vides d'air qui ont alors été créés étaient semble-t-il, suffisants pour absorber des pressions expansives dues à la formation de glace.

La réaction à la précontrainte latérale était différente pour le béton fracturé et pour le béton non fracturé. Bien que l'augmentation de la précontrainte se soit traduite, dans tous les cas, par une diminution des fuites, l'effet était plus marqué dans le cas du béton fracturé. Toutefois, le diamètre intersticiel moyen déterminé par la diffusion de gaz n'a pas subi de changement important, parce que les fuites dans le béton fracturé sont demeurées très minimes.

L'armature d'acier n'a pas eu une grande incidence sur la perméabilité des petits spécimens.

La teneur en humidité a grandement influencé le passage du gaz à travers le béton. L'humidité libre a constitué un obstacle à l'écoulement du gaz, agissant presque comme un solide. C'est un élément important, parce que le vieillissement du béton entraîne une diminution de l'humidité libre.

La vitesse des impulsions ultrasoniques a semblé varier avec la teneur en humidité et la porosité du béton, comme pour la perméabilité au gaz, ce qui laisse supposer qu'elle serait efficace pour surveiller sur place le béton des enceintes de confinement des réacteurs.

TABLE OF CONTENTS

ABSTRACT i
RÉSUMÉ ii
TABLE OF CONTENTS iii
LIST OF TABLES v
LIST OF FIGURES vi
LIST OF SYMBOLS viii
1. INTRODUCTION 1
2. SIMULATION OF CONSTRUCTION DEFECTS AND AGING BY MEANS OF FREEZE-THAW CYCLES 5
2.1 Freezing Mechanisms 6
2.1.1 Hydraulic pressure 6
2.1.2 Osmotic pressure 6
2.2 Permeability Measurements 7
2.3 Results 9
3. HUMIDITY EXPERIMENTS 10
3.1 Instrumentation 11
3.2 Alternative Pressure Measurements 11
3.2.1 The KEMA apparatus 14
4. WATER PERMEABILITY TESTS 14
5. GAS DIFFUSION THROUGH PLAIN CONCRETE 20
5.1 Diffusivity as Influenced by Pressure Gradient and Confining Pressure 21
5.2 The Influence of Confining Pressure σ_3 21
5.3 Estimation of Pore Radius in Relation to Mass Transfer of Gas 28
5.3.1 Estimation of pore size from adsorption data 31
5.3.2 Estimation of hydraulic mean radius 32
5.3.3 Estimation of pore size from gas flow characteristics. 34
6. TESTS ON THE INFLUENCE OF REINFORCING STEEL 35
6.1 Specimens 35
6.2 Experimental 35
6.3 Results 36
7. INFLUENCE OF LATERAL PRESSURE ON WATER AND GAS PERMEANCE OF CONCRETE 37
8. ULTRASONIC PULSE VELOCITY (USPV) AND PERMEANCE 38
8.1 USPV and Porosity 38
8.2 USPV and Moisture Content 39
8.3 USPV and Water/Cement Ratio w_o 40
8.4 USPV and Gas Permeability 40
8.5 Summary 42

TABLE OF CONTENTS

9. INFLUENCE OF AEROSOLS ON GAS PERMEABILITY 43
10. MASS TRANSFER RATES OF GAS AND WATER IN BEST AND WORST CASES 45
11. REFERENCES 47

APPENDICES:

VOLUME DISTRIBUTION OF PHASES IN CONCRETE — APPENDIX A

COMMENTARY ON THE SIGNIFICANCE AND DERIVATION OF THE PERMEABILITY COEFFICIENTS k AND D* — APPENDIX B

MEASURED WATER FLOW RATES AS INFLUENCED BY CONFINING PRESSURE AND PRESSURE GRADIENT — APPENDIX C

NITROGEN DIFFUSION COEFFICIENTS AS INFLUENCED BY CONFINING PRESSURE AND PRESSURE GRADIENT — APPENDIX D

A DERIVATION OF THE PERMEABILITY FLOW MEASUREMENT METHOD FOR CALCULATING MEAN PORE RADIUS a* — APPENDIX E

LIST OF TABLES

Table	Subject	Page
1	Nitrogen diffusion coefficients for freeze-thaw specimens	9
2	Average values of water permeability for constant water/cement ratio, variable porosity	18
3	Average values of water permeability for constant initial porosity and variable water/cement ratio	19
4	Comparison of latest water permeability data with previous work done on comparable concrete mixes	20
5	Twelve combinations of upstream pressure and confining pressure, for each moisture content, for each specimen	21
6	Linear regression constants of the equation $D_n^* = A+B(\Delta P/P_o)$, based on data in Appendix D	22
7	Average values of D* for specimens of constant water/cement ratio and varing porosity	26
8	Average values of D* for specimens of constant initial porosity and various water/cement ratios	26
9	Linear regression constants of the equation $D^* = P+Q(\sigma_3)$, for various porosities and water/cement ratios	28
10	Some values of the constants calculated by Gregg and Sing	33
11	Values of mean pore radius a* calculated from linear regression constants	34
12	Reinforcement configurations used for gas permeability specimens	36
13	Nitrogen diffusion coefficients of reinforced specimens, interpolated at various moisture contents	37
14	Nitrogen permeability vs. surface treatment, for various specimens	44

LIST OF FIGURES

Figure	Title	Page
1	Effect of aging shown by sorption isotherms and pore-size distribution curves	2
2	Soap leakage tests on CANDU containment structures	3
3	Soap leakage tests on CANDU containment structures	4
4	Soap leakage tests on CANDU containment structures	4
5	Schematic diagram of low-pressure permeability apparatus	7
6a,b	Photographs of low-pressure permeability apparatus	8
7	Circuit diagram for humidity sensing apparatus	12
8	Humidity sensor ready for service alongside 3 mm stock	13
9	Planetary arrangement for simultaneous anodising of 20 slugs	13
10	KEMA assembly for gas diffusion measurement	15
11	Schematic of triaxial apparatus used for high pressure water and gas permeability testing	16
12a,b	Photographs of triaxial cell and specimens	17
13	Linear fits of normalized permeability vs. normalized pressure, for constant w_o = 0.42, σ_3 = 10 MPa and variable porosity	23
14	Linear fits of normalized permeability vs. normalized pressure, for constant w_o = 0.42, σ_3 = 15 MPa and variable porosity	23
15	Linear fits of normalized permeability vs. normalized pressure, for constant w_o = 0.42, σ_3 = 25 MPa and variable porosity	24
16	Linear fits of normalized permeability vs. normalized pressure, for constant porosity ε_t = 16%, σ_3 = 10 MPa and variable water/cement ratio	24
17	Linear fits of normalized permeability vs. normalized pressure, for constant porosity ε_t = 16%, σ_3 = 15 MPa and variable water/cement ratio	25
18	Linear fits of normalized permeability vs. normalized pressure, for constant porosity ε_t = 16%, σ_3 = 25 MPa and variable water/cement ratio	25
19	Linear fits of average permeability vs. lateral confining pressure σ_3, for w_o = 0.42 and variable porosity	27

LIST OF FIGURES

Figure	Title	Page
20	Linear fits of average permeability vs. lateral confining pressure for ε_t = 16%, and variable water/cement ratio	27
21	Schematic of pore filling by products of hydration	29
22	Model pore systems in cement paste	30
23	Sorption at constant temperature, and differential pore size distribution curves	32
24	Variation of USPV with porosity for dry and saturated concrete	39
25	Variation of USPV with moisture content	40
26	Variation of USPV with w_o, for constant porosity specimens	41
27	Relationship between permeability and USPV for severely cracked and slightly cracked specimens, at various moisture contents	41
28	Relationship between USPV and permeability for different specimens, at equilibrium moisture content	42

LIST OF SYMBOLS

A	cross-sectional area
C	cement content of concrete, kgm^{-3}
D*	specific permeability or diffusivity of porous medium
D_n^*	normalized permeability
E	elastic modulus
EMC	equilibrium moisture content
$\Delta P, P$	applied pressure
P_o	reference or atmospheric pressure
P_s	saturation vapour pressure
Q	volume flow rate
R	gas constant
T	absolute temperature
USPV	ultrasonic pulse velocity
V	volume
V_m	monolayer capacity of cement paste per unit mass of cement
W	water content of cement or concrete, kgm^{-3}
$a^*, \bar{a}$	mean pore radius from gas flow characteristics
d/2	hydraulic mean radius
d_{eff}	effective pore diameter
d_p	pore diameter
Δh	pressure head
k	permeability coefficient, non-specific ($= D^*/\mu$)
ℓ	path length or thickness of specimen
r^2	correlation coefficient
r_k	Kelvin radius
t	thickness of adsorbed film
w_e	mass ratio of evaporable water per unit of cement

LIST OF SYMBOLS

w_n	mass ratio of non-evaporable water
w_o	mass ratio of total water per unit of cement
α^*	ultimate mass fraction of hydrated cement
ε_i	initial porosity, volume percent
ε_t	final porosity at test, volume percent
ϕ	liquid/solid contact angle
γ	surface tension of condensed water
ρ	density
μ	fluid viscosity
Σ_{BET}	specific surface area of cement paste, as determined by BET method
σ_3	lateral confining stress

GAS AND WATER PERMEABILITY OF CONCRETE FOR REACTOR BUILDINGS --
SMALL SPECIMENS

1. INTRODUCTION

In the first part of this investigation [Ref. 1] certain characteristics of concrete mixes were identified as having more or less influence on water, water vapour and gas permeability. It was concluded that the initial porosity was of over-riding importance and that traditional quality indices such as strength and water/cement ratio had relatively little influence on performance though all three parameters and the cement content were linked by the overall water demand of dry ingredients. These findings differed significantly from a prognosis based on current literature which places undue influence on water/cement ratio.

It was also found that water permeability was a function of the direction of flow relative to the direction of casting. Water permeability decreased with increase in confining pressure (i.e. prestress in the prototype) and this influence was maximum when the lateral pressure tended to close vertical bleeding cavities.

The laboratory specimens were made with specially designed cohesive mixes which were compacted and treated in such a way as to minimise random defects. They thus represented a state of perfection unattainable on the construction site.

In spite of this, similar defects such as invisible bleeding cavities occurred even in laboratory concrete and it was possible to influence flow rate by externally applied stresses.

The measured permeabilities for even the most porous concrete were very low and approximated values for hard, sound rock [Ref. 2]. Field concrete of this quality would provide an adequate barrier against forseeable contingencies.

Although these results were of considerable academic interest, their extrapolation to the prototype scale was inhibited by the very large discrepancies between the least favourable laboratory values and known field characteristics. For example, k values of 0.5 to 5.0 x 10^{-12} ms^{-1} for laboratory samples should be compared with values of about 10 times

greater for cores taken from the field [Ref. 3] and with free-flowing leakage tests in recently constructed CANDU reactor buildings [Ref. 4].

Typical construction defects were recognized as: cavities due to incomplete compaction; thermally induced cracks due to heat of hydration at early ages; continuous vertical bleeding passages; bleeding cavities beneath aggregates and reinforcing steel; plastic settlement cracks; horizontal slip-forming cracks; vertical slip-forming cracks due to movement of jacking rods, and unintentional variations of mix portions. It was also recognized that latent defects, usually in the form of incipient cracks due to plastic settlement which were invisible when the structure was accepted, might develop in time, as the concrete suffered drying shrinkage and cycles of loading and temperature.

Aging effects were considered common to all concrete however perfect. Even concrete stored under water displayed reduction in internal surface area due to aging alone [Refs. 3,4] and without change in porosity. Since a measure of pore size is the hydraulic mean radius defined as pore volume divided by surface area, this means that average pore size increases as a function of aging once hydration has ceased. This is illustrated in Figure 1. Calculations of hydraulic mean radius from hydration parameters are discussed in Appendix A.

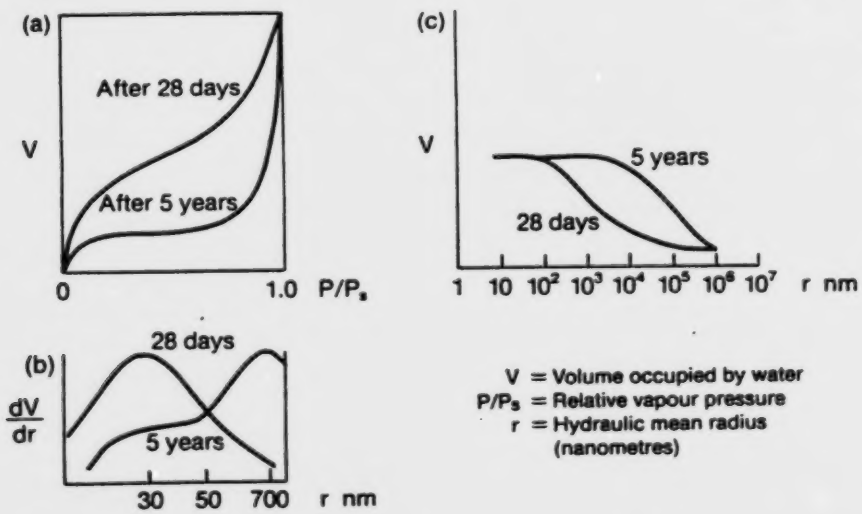

Figure 1 Effect of aging shown by (a) sorption isotherm and (b), (c) pore size distribution curves. Before aging the hydraulic mean radius ≈ 166 nm and after aging it ≈ 600 nm.

If the effects of thermal and stress cycling and wetting and drying are superimposed, the basic aging effect must be accelerated and permeability further increased by microcracking.

It seems clear that though the superficial quality of concrete, as characterised by compressive strength, improves with age, the permeability must increase through propagation of macro-defects arising from construction methods and micro-defects arising from the nature of the cementing material.

Phase I and indeed the literature as a whole do not give a satisfactory account of gas permeability of concrete. The work of Loughborough [Ref. 5] in 1966 is still widely quoted as authoritative together with that of Ludwig and Dahr [Ref. 6]. More recently the paper published by Figg [Ref. 7] has received some acceptance although it relies on a correlation of falling head with water/cement ratio, a parameter which was shown in the first report [Ref. 1] to be almost irrelevant. A common characteristic of these gas permeability tests is that the values are unrelated, probably by some orders of magnitude, to the behaviour observed in full scale pressure tests of reactor buildings [Ref. 4]. This is illustrated by soap film leakage tests shown in Figures 2, 3 and 4.

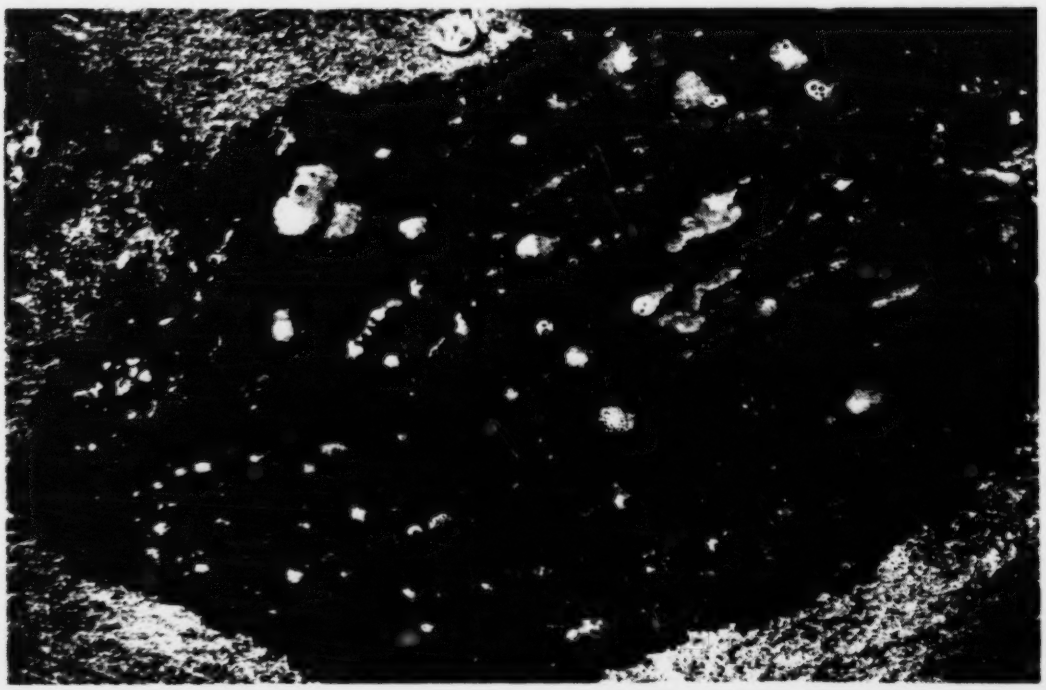

Figure 2 Soap leakage tests on CANDU containment structures [Ref. 4].

Figure 3 Soap leakage tests on CANDU containment structures [Ref. 4].

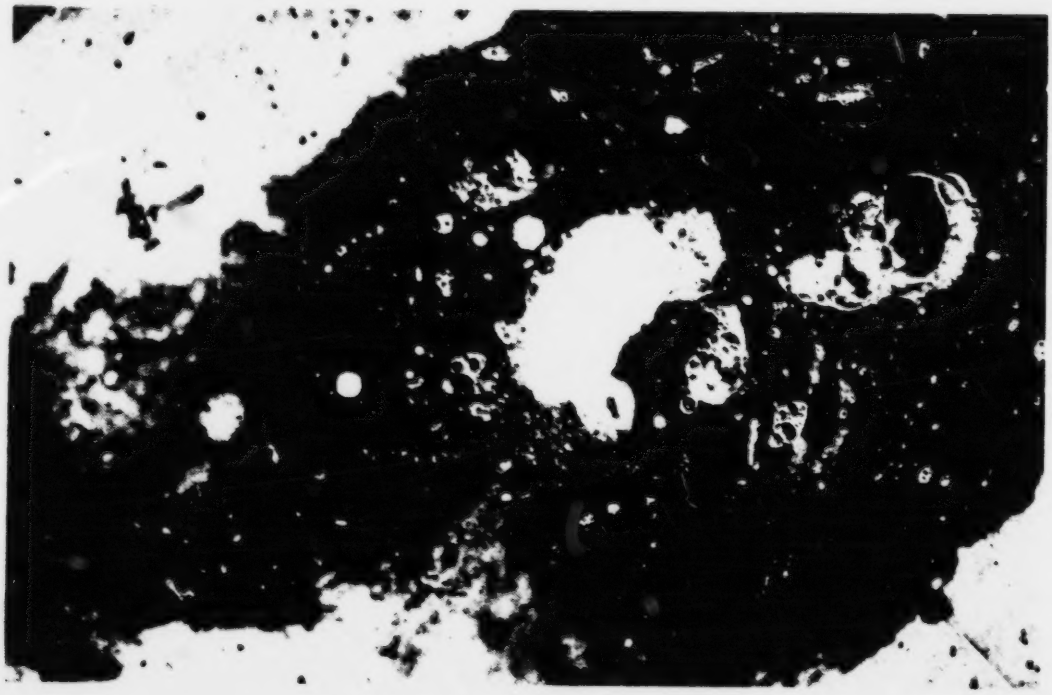

Figure 4 Soap leakage tests on CANDU containment structures [Ref. 4].

It was decided that field conditions would be simulated more closely by testing large scale specimens with a transmission length of 2 m using commercial concrete with full scale similarity in respect of steel reinforcement and aggregate size. Further, it was decided to simulate time degradation over the life of the concrete by artificial aging.

To provide guidance in the development of future prototype scale tests, a small-scale test programme was mounted to assess the following:

(1) the effect of drying shrinkage cracks on permeability;
(2) the effect of freeze-thaw damage on permeability;
(3) the influence of the volume and orientation of steel reinforcement on permeability;
(4) the influence of moisture content on mass transfer of gas; and
(5) the effects of prestress on gas permeability.

Associated with experimental determination of permeability by direct observation of mass or volume of water or gas transmitted, other indirect measures were introduced into the programme. These were transverse ultrasonic pulse velocity measurements and pore pressure sensing both of which showed promise for economical adaption to field use.

This document reports on the small-scale test programme. Results of prototype scale tests will be presented in subsequent reports.

2. SIMULATION OF CONSTRUCTION DEFECTS AND AGING BY MEANS OF FREEZE-THAW CYCLES

Construction defects and aging, which are mainly responsible for the permeance of field concrete are difficult to simulate exactly in the laboratory. Examples of the most serious defects occurring in the field are:

(1) horizontal cracks due to "stick-slip" motion of the sliding form;

(2) vertical cracks due to sideways movement of jacking rods in semi-plastic concrete;

(3) honeycombing due to incomplete compaction of concrete; and

(4) plastic shrinkage cracking due to settlement of concrete over horizontal reinforcing bars.

Such defects are not generally amenable to quantitative modelling on the laboratory scale. However, the effects of microcracking due to freeze-thaw are functionally similar to many imperfections found in the field, in that the cracks provide a connecting path between air voids allowing easier passage of the permeant, so tests were performed to investigate the effects of freeze-thaw damage on permeability.

2.1 Freezing Mechanisms

Freeze-thaw damage to non air-entrained concrete occurs when dilating pressure in ice and pore water causes tensile stresses which exceed the strength of the cement matrix. Such stresses are usually attributed to two main results of freezing.

2.1.1 Hydraulic Pressure

Ice formed in large pores expands by about 9 per cent and exerts hydrostatic pressure on the remaining liquid water, causing it to flow towards voids which can accommodate it. For a given rate of ice formation the hydraulic pressure thus generated depends on the length of flow path and the permeance of the intervening solid. In general, ice does not form in pores having a least dimension <3.6 nm until the temperature falls below -78°C [Ref. 8]. Freezing in coarse pores causes flow towards porous hydration products which are the source of strength in cement paste.

2.1.2 Osmotic Pressure

As freezing proceeds, the concentration of dissolved salts in pore water increases non-uniformly, according to the size of water-filled cavities and the degree of saturation, so that the movement of water is increased by osmotic pressure.

When the internal pressures caused by freezing exceed the tensile strength of the concrete, cracking occurs.

Concrete is normally protected against freeze-thaw damage by deliberately entraining air in the form of closely spaced spherical bubbles. Because of the close spacing, there is little resistance to the movement of water and the little hydraulic pressure which is generated is innocuous.

In the present case the concrete was deliberately made without entrained air in order to provoke cracking by freezing.

Specimens were prepared with a standard A_2 mix [Ref. 1] having cement = 548 kg m^{-3} and water = 230 kg m^{-3}. The specimens were cast in precisely machined plastic moulds measuring 150 mm diameter x 300 mm and extruded at 24 hours age. The cylinders were then sliced into 30 mm discs, which were then wiped to remove surface moisture and stored in sealed containers to simulate curing in the interior of a large mass of concrete. After 7 days the specimens were subjected to 10 freeze-thaw cycles from -10°C to +40°C.

2.2. Permeability Measurements

The permeability apparatus is shown in Figures 5 and 6.

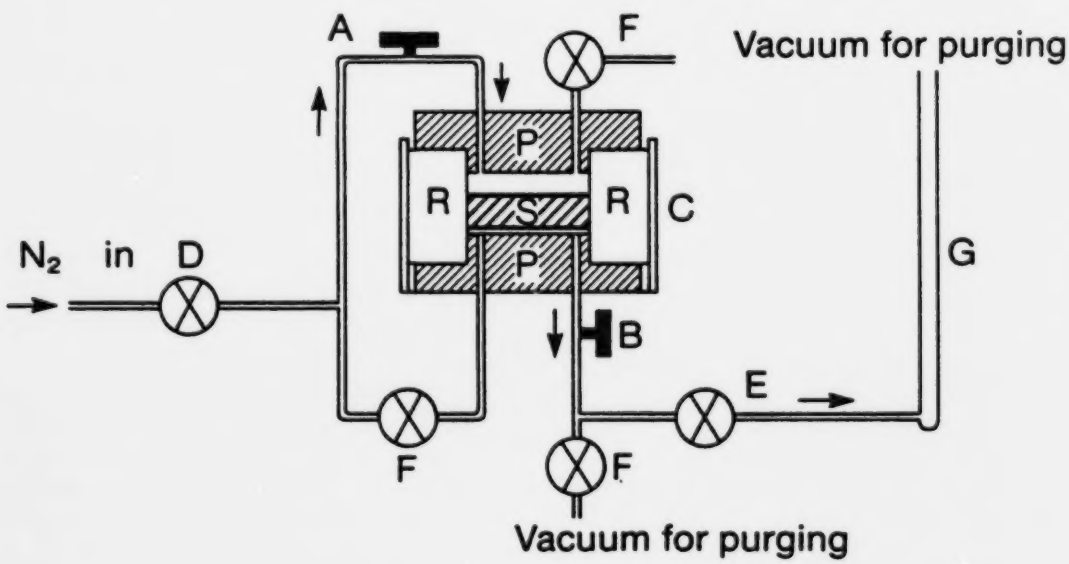

Figure 5 Schematic diagram of permeability apparatus: A. Inlet pressure transducer. B. Exit pressure transducer. C. Cell with specimen. D. Inlet valve. E. Outlet valve. F. Pressure relief valves. G. Bubble Flowmeter. The two platens P, through which the gas enters and exits the specimen compress the silicone rubber annulus R, to provide a gas-tight seal on the circumference of the specimen S.

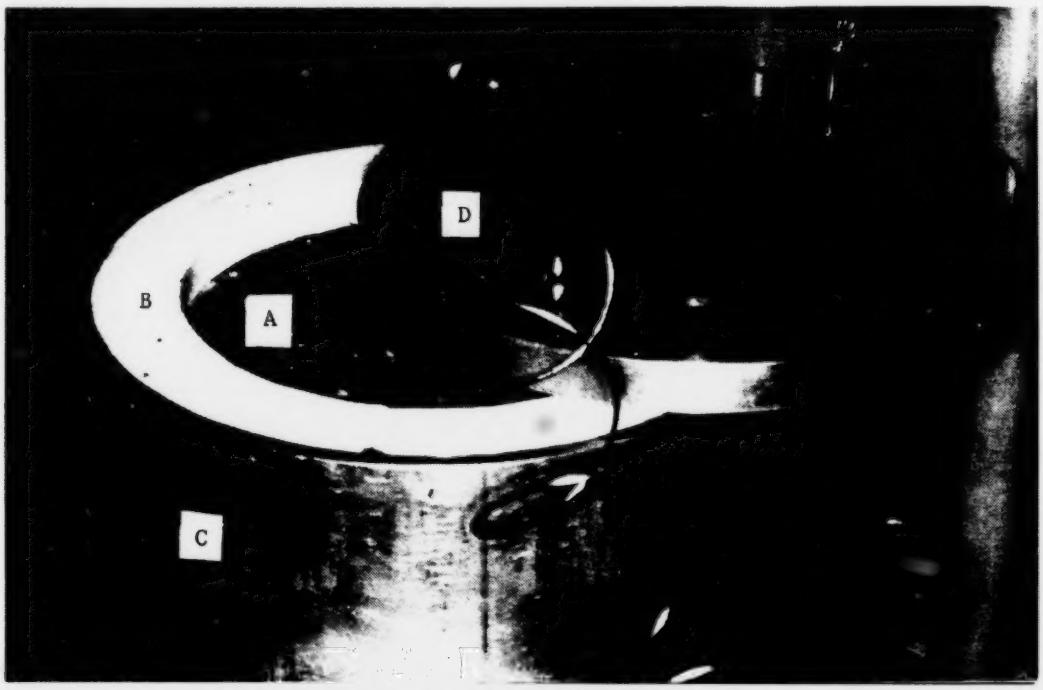

Figure 6a Low pressure permeability cell showing: A. Specimen. B. Silicone rubber seal. C. Containing ring. D. Top cover plate.

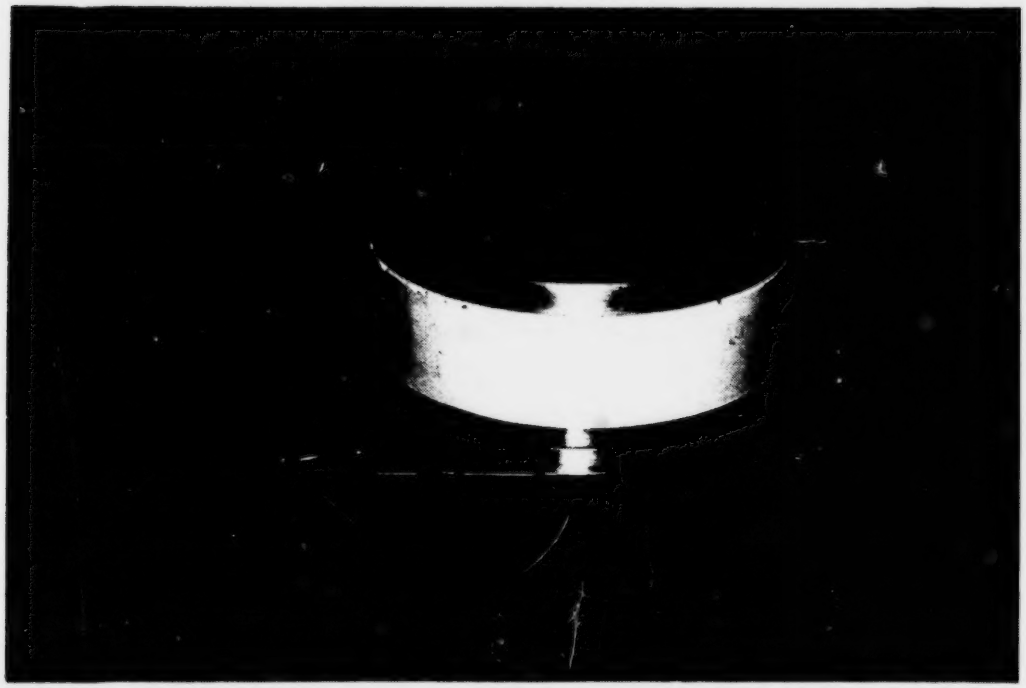

Figure 6b As above, with containing ring removed. Silicone rubber annulus is completely visible, as well as bottom cover plate and loading frame.

2.3 Results

The permeability characteristics of freeze-thaw specimens were compared with control specimens which were kept at room temperature. The results are summarized in Table 1.

It is clear from these results that the regime of freeze-thaw cycles was insufficient to cause serious cracking since there was negligible increase in the rate of gas diffusion either at equilibrium moisture content (EMC), or when the concrete was dry. When the control concrete was oven-dried from EMC, permeance increased by a factor of 153. When the control concrete was saturated before drying, this factor reduced to 71, probably

---

Table 1

Nitrogen diffusion D* through specimens subjected to simulated mass curing and 10 freeze-thaw cycles from -10 to +40°C. In this Table $D^* = \mu\ell Q/\Delta P.A$ (m^2). (See Appendix B for a derivation of the permeability coefficient D*.)

	Condition in Chronological sequence	D* $m^2/10^{16}$	Arbitrary units
Control #1	At EMC	0.031(1)	1
	Oven Dry	4.656	153
	Re-saturated	0.009	-
Control #2	At EMC	0.080	1
	Saturated	0.016	-
	Oven Dry	5.680	71
Freeze-Thaw	At EMC	0.076	1
	Saturated	0.000	-
	Oven Dry	6.230	82

EMC = Equilibrium Moisture Content when stored in sealed containers. Hydration proceeded by consumption of mixing water and resulted in some dessication.

(1) = This means 0.031×10^{-16} m^2.

due to further hydration of cement on contact with water. Similar treatment of concrete artificially aged by freeze-thaw resulted in an increase of 82 which is considered to be not significantly different from 71 in the present context.

The reason for the apparent resistance of this concrete to freeze-thaw damage is thought to be due to self-dessication. In order to simulate mass curing, gain or loss of moisture was prevented and hydration proceeded by consumption of mixing water. This is the same condition as that found at the centre of a massive block of concrete where water applied to the surface cannot penetrate the outer layers fast enough to replace the volume deficiency caused by chemical shrinkage [Ref. 9]. The empty space in the gel structure, by this mechanism, served the same purpose as air entrainment in minimising freeze-thaw damage.

It is estimated that of the original mixing water (230 volume parts per 1000 of concrete), 83 parts were consumed in the hydration process and the corresponding volume deficiency created 22 parts per thousand of air-filled space. In terms of the cement paste which occupied 400 volume parts per thousand, the volume of air was slightly more than 5 per cent. It is believed that this was sufficient to prevent frost damage and hence the desired aging effect was not achieved.

If this method of artificial aging is to be attempted again, the concrete will need to be vacuum-saturated before freezing.

3. HUMIDITY EXPERIMENTS

In a reactor building it is to be expected that different relative humidities exist on either side of the concrete barrier. Within the concrete itself the partial pressure of water vapour in the pores will depend, inter alia, on the imposed humidity gradient, the degree of hydration and pore size distribution.

In the event of damage to the concrete, for example a structural crack, or a sudden change in the humidity gradient caused by heat or pressure on one side, the partial pressure of water vapour in the pores will change from a quasi-equilibrium state to a transient state.

3.1 Instrumentation

It was thought that early warning of leakage or distress in the concrete would be reflected in the instrumentation as changes in internal vapour pressure of the concrete. To this end, humidity-sensing devices consisting of anodised aluminium slugs were developed, together with appropriate circuitry, to sense variation of resistance and capacity of the anodised layer accompanying sorption or desorption of water. The circuit diagram is shown in Figure 7. The aluminium slugs measured 3 mm diameter by 50 mm long and are shown in Figure 8.

It was found that good repeatable correlation between voltage output and relative humidity was obtained within the range 7 to 85 per cent relative humidity, i.e. $0.07 < P/P_s < 0.85$. If, at higher relative humidity, drops of water condensed on the anodised aluminium surface, the calibration was destroyed and had to be repeated.

Mass production of aluminium sensors in batches of 20 was attempted using the apparatus shown in Figure 9.

The apparatus as fabricated has each aluminium slug being rotated about its own axis by a 3 volt D.C. motor and the whole assembly rotated about the cathode through a friction drive and a 24 volt motor.

Because the anodising current was supplied to the work pieces through slip rings it proved impossible to secure the necessary stability in the current supply and further work proceeded with a static arrangement. Since the slugs could only be anodised in pairs, it meant that each sensor had to be individually calibrated.

3.2 Alternative Pressure Measurements

At this juncture AECB received a communication from Mnr. C.J. van Daatselaar,* describing some of the tests being conducted at the KEMA** laboratories in Arnhem. After consultations with the Scientific Authority [Ref. 10], the writer visited these laboratories where he found that gas

---

*Head, Nuclear Department, Directorate-general of Labour, The Netherlands

**The KEMA laboratories (NV tot Keuring van Electrotechnische Materialen) are responsible for control and inspection, research and development and Engineering and consulting for the Electric Power Authority in Arnhem, Holland.

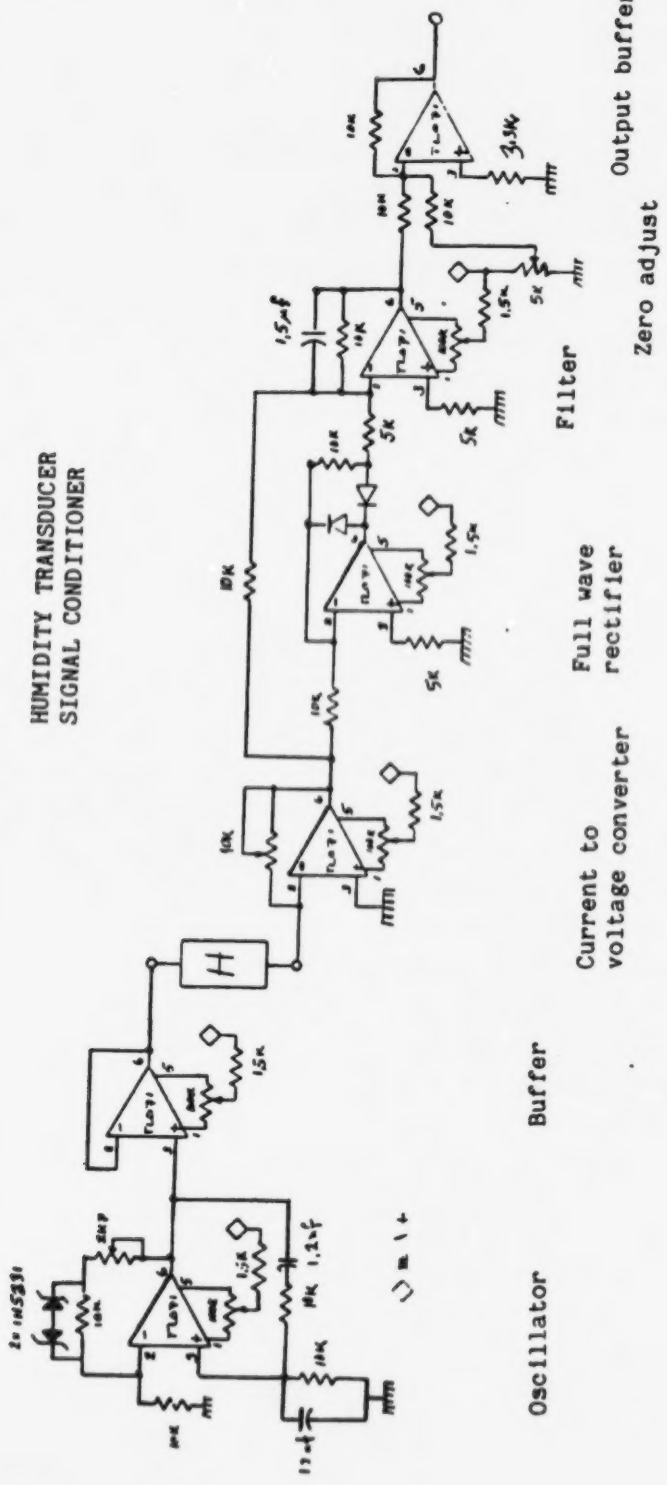

Figure 7 Circuit diagram for humidity sensing apparatus

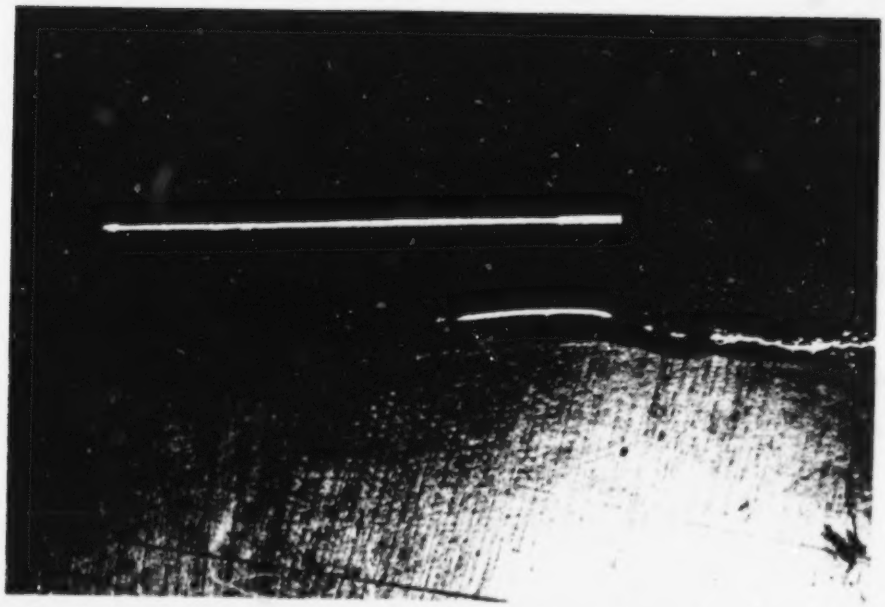

Figure 8 Humidity sensor ready for service alongside 3 mm stock.

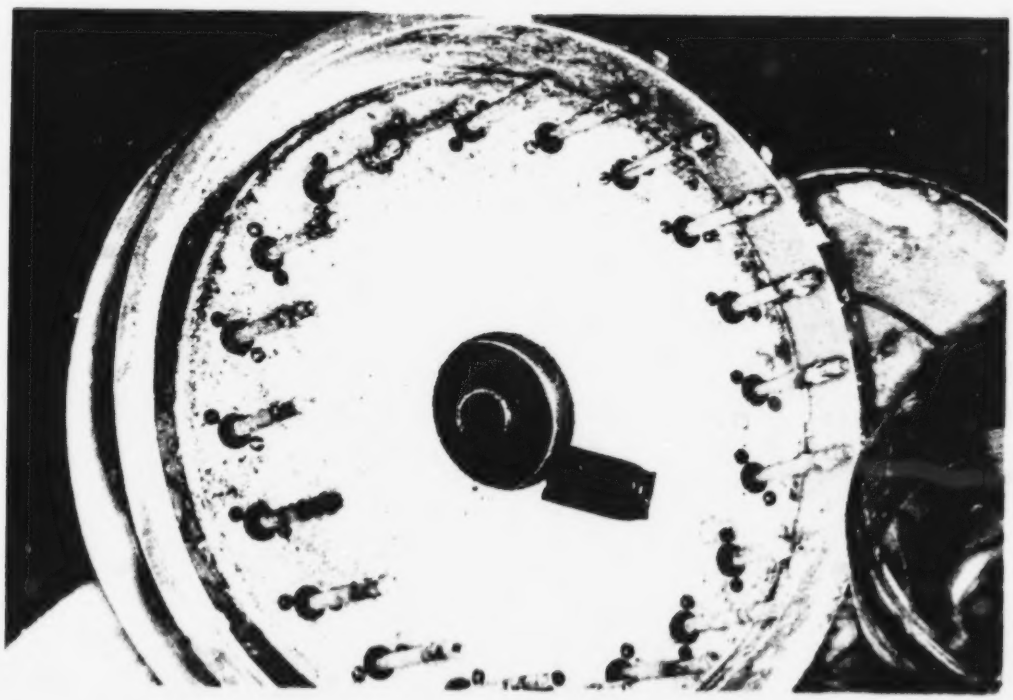

Figure 9 Planetary arrangement for simultaneous anodising of 20 slugs.

diffusion in concrete was measured by directly determining pore pressure in the concrete specimen.

3.2.1 The KEMA apparatus

The KEMA laboratories conducted their tests on concrete cores each measuring 200 mm diameter by 300 mm long, and the testing apparatus is shown in Figure 10. The cores were sealed in a concrete cylinder closed at one end. Three instrument wells were formed at depths of 10, 60 and 100 mm from the concrete face in contact with pressurised nitrogen. The test was conducted by increasing the pressure on the free face and observing the advance of the pressure front by means of transducers located in the pressure wells.

In view of the simplicity of this concept it was decided to abandon or defer P/P_s measurements in favour of direct pressure measurements and resources were diverted to the location and acquisition of suitable devices.

4. WATER PERMEABILITY TESTS

It was shown in previous work [Ref. 1] that water permeability was affected by biaxial lateral prestress σ_3. In the present series the work was extended by subjecting the specimens to artificial weathering by drying and re-saturating the concrete.

Two groups of specimens, (a) with varying initial porosity and constant water/cement ratio and (b) with varying water/cement ratio and constant porosity were cast in 150 mm diameter x 300 mm molds. After 7 days 3 cores 54 mm diameter each, were drilled parallel to the longitudinal axis and these were cut into 50-55 mm lengths.

The specimens were then subjected to drying in a vacuum oven at zero per cent relative humidity and gradually increasing the temperature to 100°C. After re-saturation under vacuum, the specimens were tested in a Hoek triaxial cell arrangement, as shown in Figures 11 and 12. This apparatus was also used to obtain the permeability data presented in INFO 0111 [Ref. 1].

The results for each test, including pressure gradient and flow rate data are to be found in Appendix C, and Appendix B explains the significance of the two permeability coefficients, k and D*.

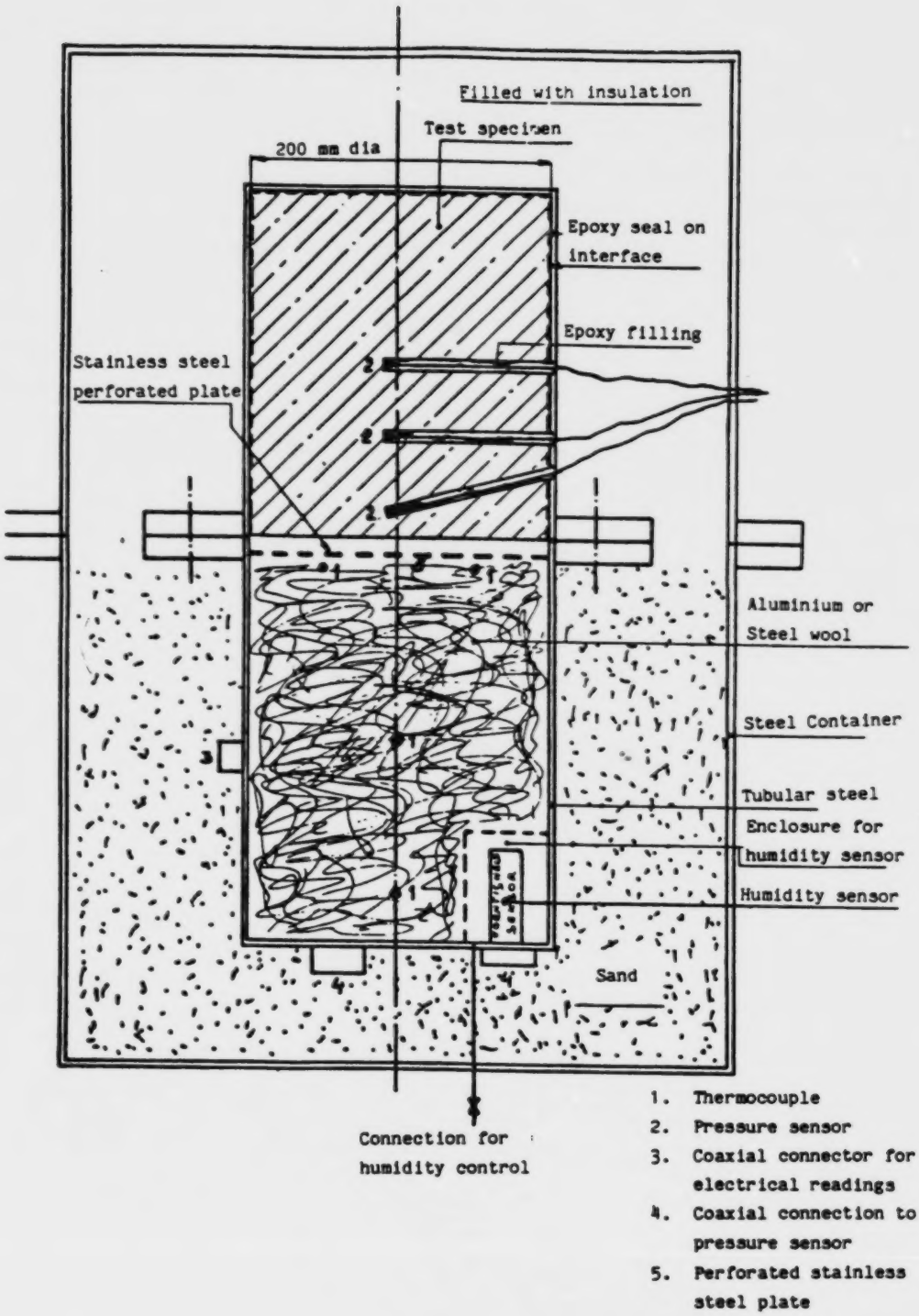

Figure 10 KEMA assembly for gas diffusion measurement [Ref. 10]

These results do not accord with the fundamental principle upon which D'Arcy's law is based, viz., that the coefficient of permeability k is invariant with the hydraulic gradient $\Delta h/\ell$. However, if the values of k are averaged for the experimental range of $\Delta h/\ell$, the standard deviations are similar to those found elsewhere [Refs. 1,3].

Such averages, as calculated from the data in Appendix C, are presented in Tables 2 and 3 along with their standard deviations, and Table 4 compares these results with those of comparable concrete mixes reported in INFO 0111 [Ref. 1].

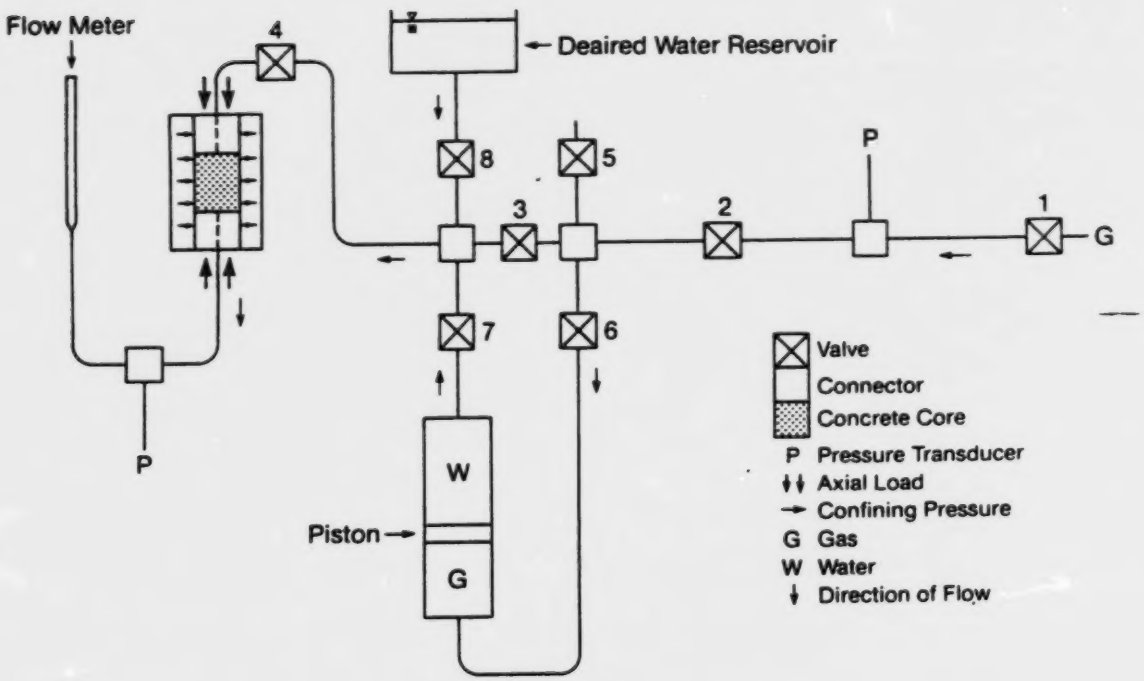

Figure 11 Schematic of triaxial apparatus used for high pressure water and gas permeability testing.

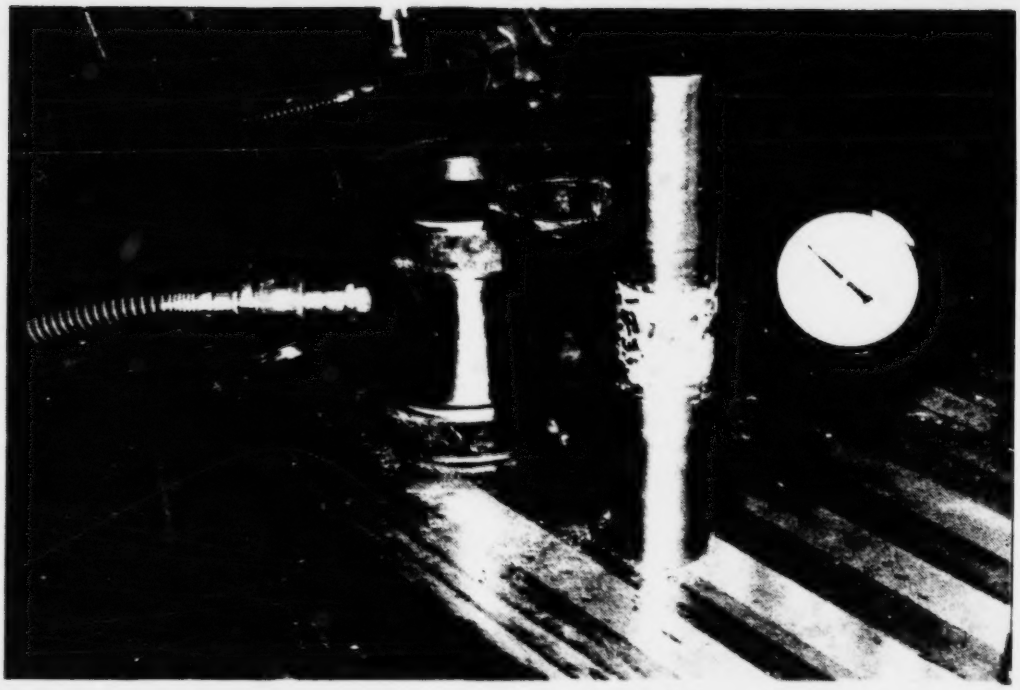

Figure 12a Left to right: triaxial cell showing hydraulic fittings; rubber membrane which encloses specimen during testing; specimen between stainless steel loading heads.

Figure 12b Close-up of cylindrical specimen between stainless loading heads, which apply an axial load as well as providing a passageway for gas or liquid permeants.

Table 2

Average values of water permeability for constant water/cement ratio w_o, variable porosity ε and varying confining pressure σ_3. Values in parenthesis are standard deviations. (See Appendix B for a derivation of the permeability coefficients k and D*.)

w_o	ε_i%	ε_t%	σ_3 (MPa)	$k/10^{12}$ m/s	$D^*/10^{18}$ m^2
0.42	29.2	18.0	5	137 (82)[+]	12.7[++]
			10	102 (17)	9.5
			15	68 (5)	6.3
0.42	23.0	16.7	5	44 (12)	4.1
			10	31 (15)	2.9
			15	16 (5)	1.5
0.42	17.6	11.0	5	0.3 (1.2)	.03
			10	0.3 (OOR)	.03
			15	0.1 (.10)	.01
0.42	15.0	10.0	5	2.0 (0.9)	0.2
			10	1.0 (0.39)	0.1
			15	0.6 (0.42)	.06

ε_i = initial porosity of fresh concrete
ε_t = porosity at time of test
OOR = out of range -- standard deviation high with respect to average value

[+] Read as 137×10^{-12} m/s
[++] Read as 12.7×10^{-18} m^2

Table 3

Average values of water permeability for constant initial porosity, variable water/cement ratio w_o, and variable confining pressure σ_3. Values in parenthesis are standard deviations.

w_o	ε_i%	ε_t%	σ_3 (MPa)	$k/10^{12}$ m/s		$D^*/10^{18} m^2$
0.42	23.0	16.7	5	44	(12)[+]	4.1[++]
			10	31	(16)	2.9
			15	16	(5)	1.5
0.56	23.0	15.8	5	80	(OOR)[+++]	7.4
			10	34	(5.3)	3.2
			15	14	(3.5)	1.3
0.64	23.0	15.9	5	5	(0.93)	0.5
			10	5	(OOR)	0.5
			15	7	(OOR)	0.7
0.77	23.0	15.7	5	5	(0.21)	0.5
			10	3	(0.44)	0.3
			15	2	(0.79)	0.2

Notes: [+] Read as 44×10^{-12} m/s

[++] Read as 4.1×10^{-18} m^2

[+++] Out of range - standard deviation high with respect to average value.

Table 4

Comparison of latest water permeability data with previous work done on comparable concrete mixes.

			This Report		INFO 0111 [Ref. 1]	
w_o	ε_i%	σ_3MPa	$k/10^{12}$m/s	$D^*/10^{18}m^2$	$k/10^{12}$m/s	$D^*/10^{18}$ m^2
0.42	23.0	10	31[+]	2.9[++]	4.4	0.41
		15	16	1.5	3.2	0.30
0.42	17.6	10	0.3	.028	2.6	0.24
		15	0.1	.009	1.9	0.18
0.42	15.0	10	1.0	.093	1.9	0.18
		15	0.6	.055	1.4	0.13

Notes: [+] Read as 31 x 10^{-12} m/s.
[++] Read as 2.9 x 10^{-18} m^2.

5. GAS DIFFUSION THROUGH PLAIN CONCRETE

Low pressure gas diffusion is discussed in Section 6, particularly in the context of reinforced concrete. This section deals with gas permeability at higher pressures, on unreinforced concrete of two types: (a) where water/cement ratio is kept constant and initial porosity varied; and (b) where porosity was kept constant and water/cement ratio varied.

The tests were carried out in a Hoek triaxial cell exactly as described in Section 4 on water permeability, except that the permeant was nitrogen at room temperature and the measurement of the quantity of gas was by means of a gas burette.

It was found necessary to test the concrete at each of four different moisture contents in order to establish interdependance of gas flow and empty pore space.

For each moisture content, twelve combinations of pressure gradient and confining pressure were imposed as detailed in Table 5.

Table 5

Twelve combinations of upstream pressure and confining pressure for each moisture content, for each specimen.

Confining Pressure σ_3 (MPa)	Upstream Pressure (MPa)			
	0.69	1.38	2.76	5.52
10	1	2	3	4
15	5	6	7	8
25	9	10	11	12

5.1 Diffusivity as Influenced by Pressure Gradient and Confining Pressure

Appendix D gives values of the diffusivity coefficient $D^*(m^2)$ as influenced by driving pressure ΔP and confining pressure σ_3 for concretes of various initial porosities and water/cement ratios.

It was decided to reduce all following considerations to data normalised by interpolation to 70 per cent moisture loss.

It can be seen that for constant w_o, ε_i and σ_3, D^* generally increased with ΔP. Plots of D^* against ΔP, in the normalized form of $D^*/(\mu/P_o)$ vs. $\Delta P/P_o$, where μ is the viscosity of nitrogen and P_o is atmospheric pressure, are shown in Figures 13 to 18. A linear relationship can be seen to exist, and the effects of porosity and water/cement ratio at a given confining pressure are graphically illustrated.

Constants of the linear regression equations are given in Table 6. The linear approximation to the experimental data was generally satisfactory.

5.2 The Influence of Confining Pressure σ_3

The data in Appendix D was used to obtain average values of D^* for varying σ_3 for each of the 7 mixes, at 70% moisture loss. These results are given in Tables 7 and 8 and graphed in Figures 19 and 20. It is seen that values

Table 6

Solutions of the equation $D_n^* = A + B(\Delta P/P_o)$ where $D_n^* = D^*/(\mu/P_o)$ and ΔP = MPa pressure. A and B are constants and $\Delta P/P_o$ is the normalized upstream pressure and r^2 = correlation coefficient. Test data was normalised at 70 per cent moisture loss.

6-1 Constant water/cement ratio = 0.42 and varying porosity

Specimen	w_o	ε_i%	ε_t%	σ_3 MPa	$A(m^2/s)/10^6$	$B(m^2/s)/10^6$	r^2
A_1	0.42	29.2	18.0	10	2.47	.041	0.50
				15	2.15	.030	0.54
				25	1.31	.037	0.89
A_2	0.42	23.0	16.7	10	0.30	.029	1.00
				15	0.24	.025	1.00
				25	0.20	.013	0.99
A_3	0.42	17.6	11.0	10	0.14	.01	0.96
				15	0.15	.008	0.97
				25	0.11	.009	1.00
A_4	0.42	15.0	10.0	10	0.38	.050	1.00
				15	0.39	.039	0.99
				25	0.41	.027	1.00

6-2 Constant porosity and varying water/cement ratio

Specimen	w_o	ε_i%	ε_t%	σ_3 MPa	$A(m^2/s)/10^6$	$B(m^2/s)/10^6$	r^2
B_1	0.56	23.0	15.8	10	0.36	.028	0.99
				15	0.21	.027	1.00
				25	0.19	.021	0.99
B_2	0.64	23.0	15.9	10	0.59	.046	0.97
				15	0.58	.041	0.99
				25	0.53	.031	0.99
B_3	0.77	23.0	15.7	10	0.36	.038	0.99
				15	0.35	.030	1.00
				25	0.29	.025	0.99

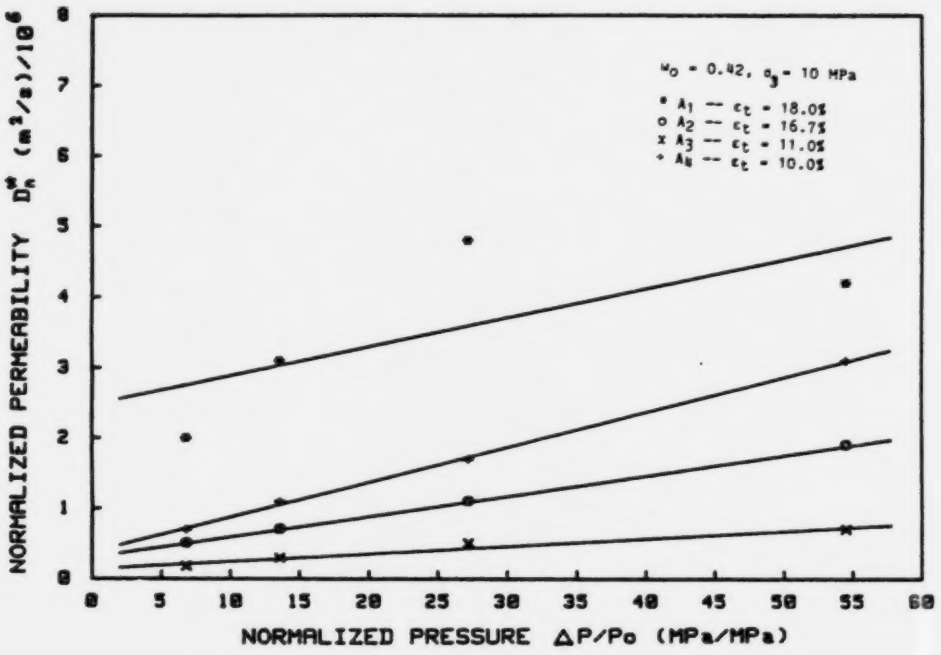
w_o = 0.42, σ_3 = 10 MPa
* A_1 — ϵ_t = 18.0%
o A_2 — ϵ_t = 16.7%
x A_3 — ϵ_t = 11.0%
+ A_4 — ϵ_t = 10.0%
NORMALIZED PERMEABILITY D_n^* (m^2/s)/10^6
NORMALIZED PRESSURE ΔP/Po (MPa/MPa)
0 1 2 3 4 5 6 7 8
0 5 10 15 20 25 30 35 40 45 50 55 60

Figure 13 Linear fits of normalized permeability vs. normalized pressure, for constant w_o = 0.42, σ_3 = 10 MPa and variable porosity.

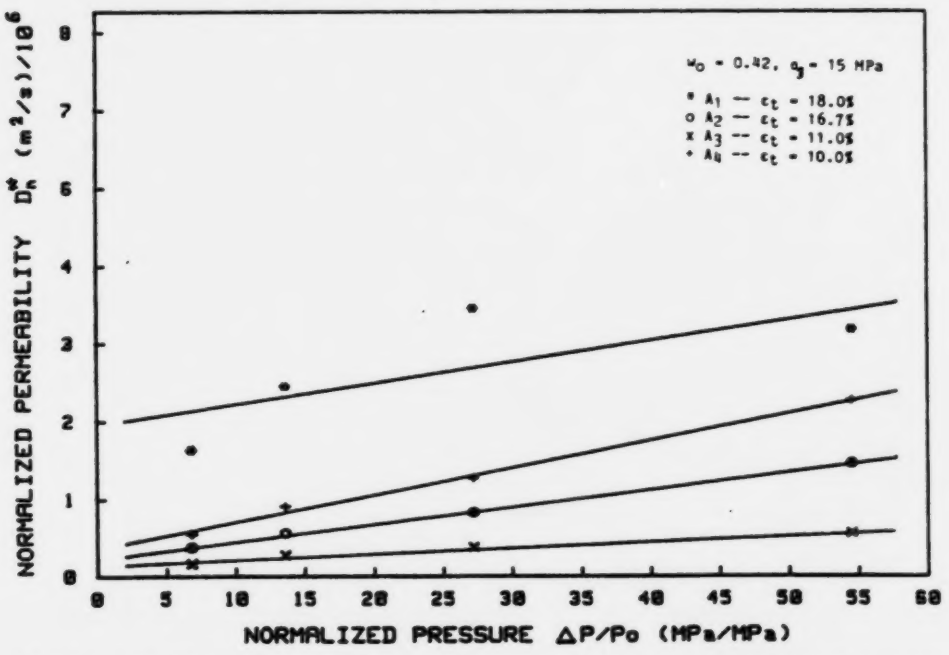
w_o = 0.42, σ_3 = 15 MPa
* A_1 — ϵ_t = 18.0%
o A_2 — ϵ_t = 16.7%
x A_3 — ϵ_t = 11.0%
+ A_4 — ϵ_t = 10.0%
NORMALIZED PERMEABILITY D_n^* (m^2/s)/10^6
NORMALIZED PRESSURE ΔP/Po (MPa/MPa)
0 1 2 3 4 5 6 7 8
0 5 10 15 20 25 30 35 40 45 50 55 60

Figure 14 Linear fits of normalized permeability vs. normalized pressure, for constant w_o = 0.42, σ_3 = 15 MPa and variable porosity.

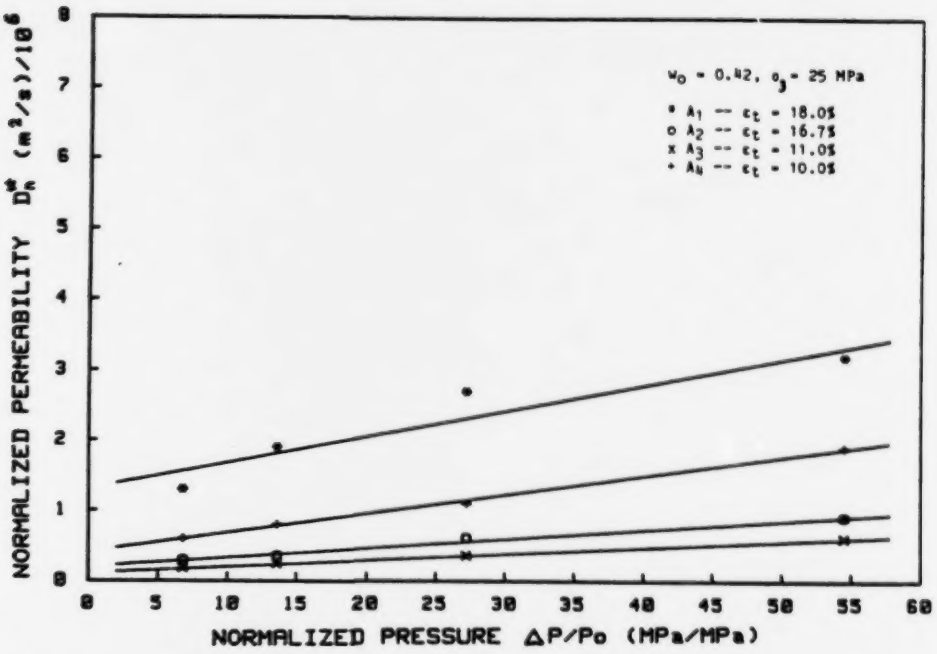
w_o = 0.42, σ_3 = 25 MPa
* A_1 -- ε_t = 18.0%
o A_2 -- ε_t = 16.7%
x A_3 -- ε_t = 11.0%
+ A_4 -- ε_t = 10.0%
NORMALIZED PERMEABILITY D_n^* (m^2/s)/10^6
NORMALIZED PRESSURE $\Delta P/P_o$ (MPa/MPa)
0 5 10 15 20 25 30 35 40 45 50 55 60
0 1 2 3 4 5 6 7 8

Figure 15 Linear fits of normalized permeability vs. normalized pressure, for constant w_o = 0.42, σ_3 = 25 MPa and variable porosity.

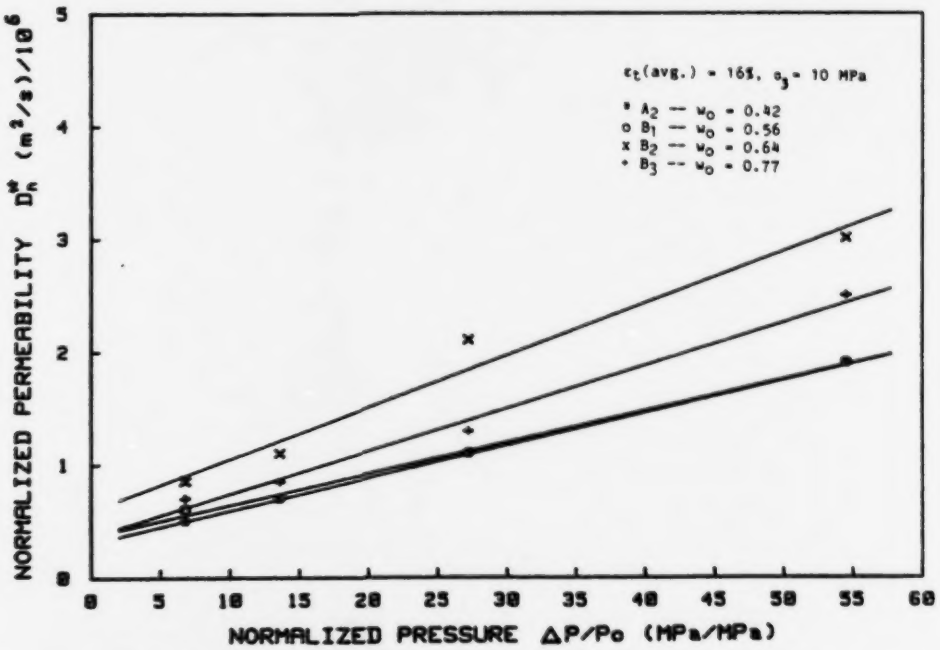
ε_t(avg.) = 16%, σ_3 = 10 MPa
* A_2 -- w_o = 0.42
o B_1 -- w_o = 0.56
x B_2 -- w_o = 0.64
+ B_3 -- w_o = 0.77
NORMALIZED PERMEABILITY D_n^* (m^2/s)/10^6
NORMALIZED PRESSURE $\Delta P/P_o$ (MPa/MPa)
0 5 10 15 20 25 30 35 40 45 50 55 60
0 1 2 3 4 5

Figure 16 Linear fits of normalized permeability vs. normalized pressure, for constant porosity ε_t = 16%, σ_3 = 10 MPa and variable water/cement ratio.

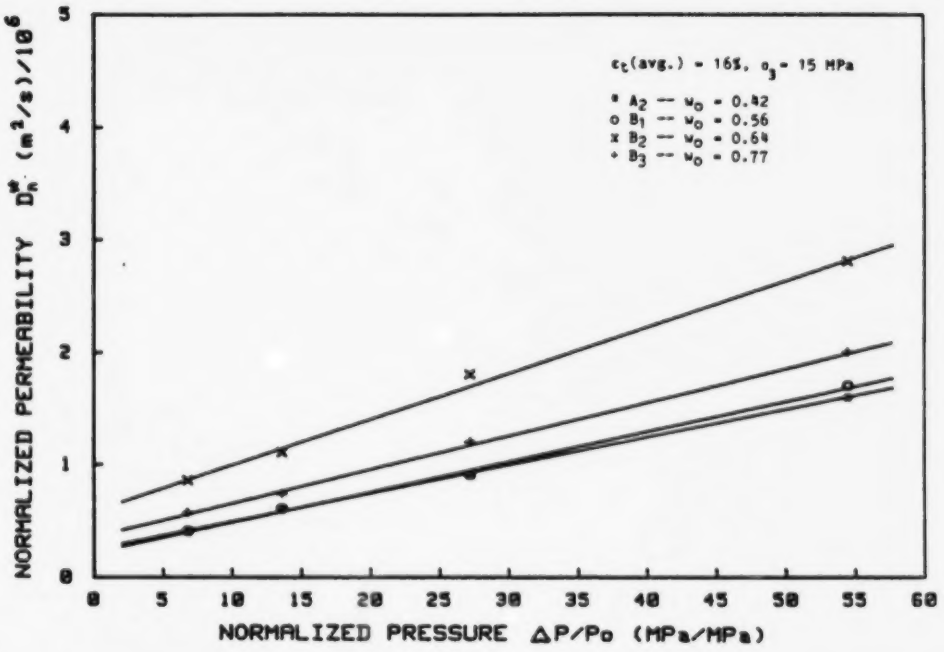
ε_t(avg.) = 16%, σ_3 = 15 MPa
* A_2 — w_o = 0.42
o B_1 — w_o = 0.56
x B_2 — w_o = 0.64
+ B_3 — w_o = 0.77
NORMALIZED PERMEABILITY D_n^* (m^2/s)/10^6
NORMALIZED PRESSURE $\Delta P/P_o$ (MPa/MPa)
0 1 2 3 4 5
0 5 10 15 20 25 30 35 40 45 50 55 60

Figure 17 Linear fits of normalized permeability vs. normalized pressure, for constant porosity ε_t = 16%, σ_3 = 15 MPa and variable water/cement ratio.

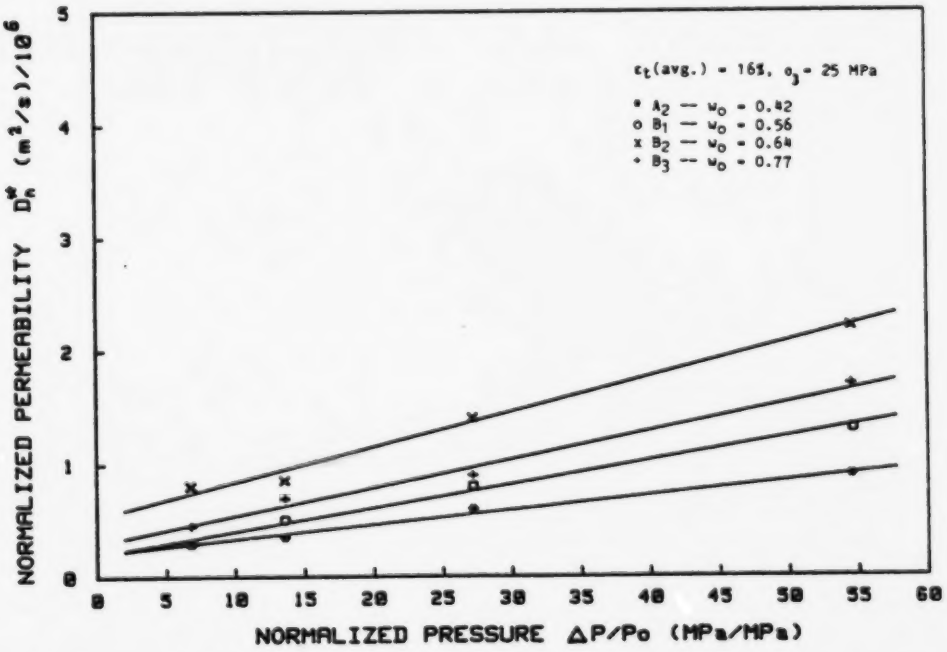
ε_t(avg.) = 16%, σ_3 = 25 MPa
* A_2 — w_o = 0.42
o B_1 — w_o = 0.56
x B_2 — w_o = 0.64
+ B_3 — w_o = 0.77
NORMALIZED PERMEABILITY D_n^* (m^2/s)/10^6
NORMALIZED PRESSURE $\Delta P/P_o$ (MPa/MPa)
0 1 2 3 4 5
0 5 10 15 20 25 30 35 40 45 50 55 60

Figure 18 Linear fits of normalized permeability vs. normalized pressure, for constant porosity ε_t = 16%, σ_3 = 25 MPa and variable water/cement ratio.

Table 7

Average values of D^* normalized to 70 per cent moisture loss, for specimens of constant water/cement ratio and various porosities.

	Porosity: Volume Per Cent			
w_o	ε_i	ε_t	σ_3 (MPa)	D^* $m^2/10^{16}$
0.42	29.2	18.0	10	6.2
			15	5.2
			25	4.0
0.42	23.0	16.7	10	1.8
			15	1.5
			25	0.9
0.42	17.0	11.0	10	0.7
			15	0.6
			25	0.6
0.42	14.0	10.0	10	2.9
			15	2.4
			25	1.9

Table 8

Average values of D^* normalized to 70 per cent moisture loss, for specimens of constant initial porosity and various water/cement ratios.

	Porosity: Volume Per Cent			
w_o	ε_i	ε_t	σ_3 (MPa)	D^* $m^2/10^{16}$
0.42	23.0	16.7	10	1.8
			15	1.5
			25	0.9
0.56	23.0	15.8	10	1.9
			15	1.6
			25	1.3
0.64	23.0	15.9	10	3.1
			15	2.9
			25	2.3
0.77	23.0	15.7	10	2.3
			15	2.0
			25	1.7

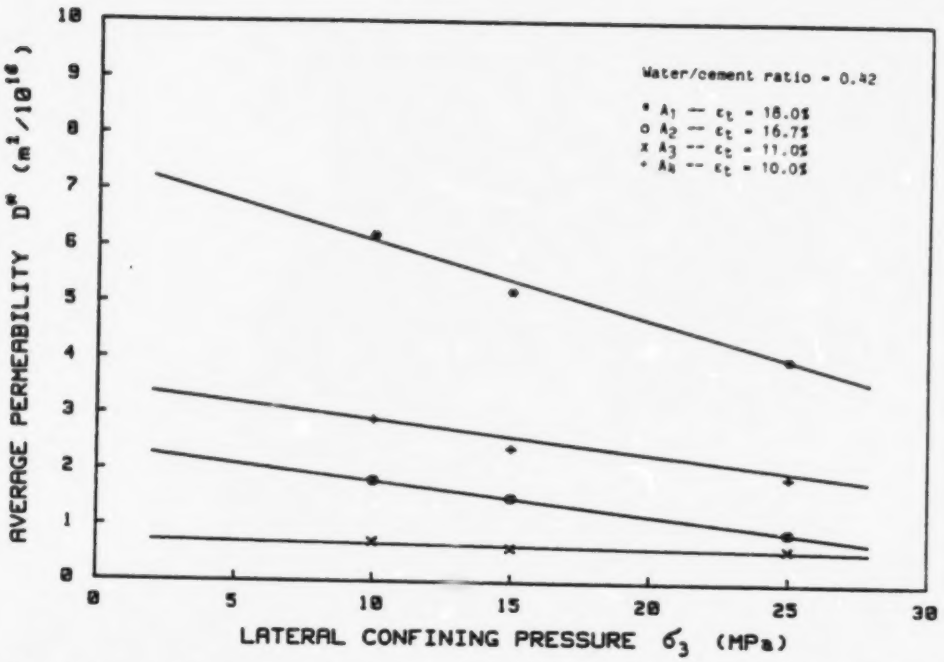

Figure 19 Linear fits of average permeability vs. lateral confining pressure σ_3, for w_o = 0.42 and variable porosity.

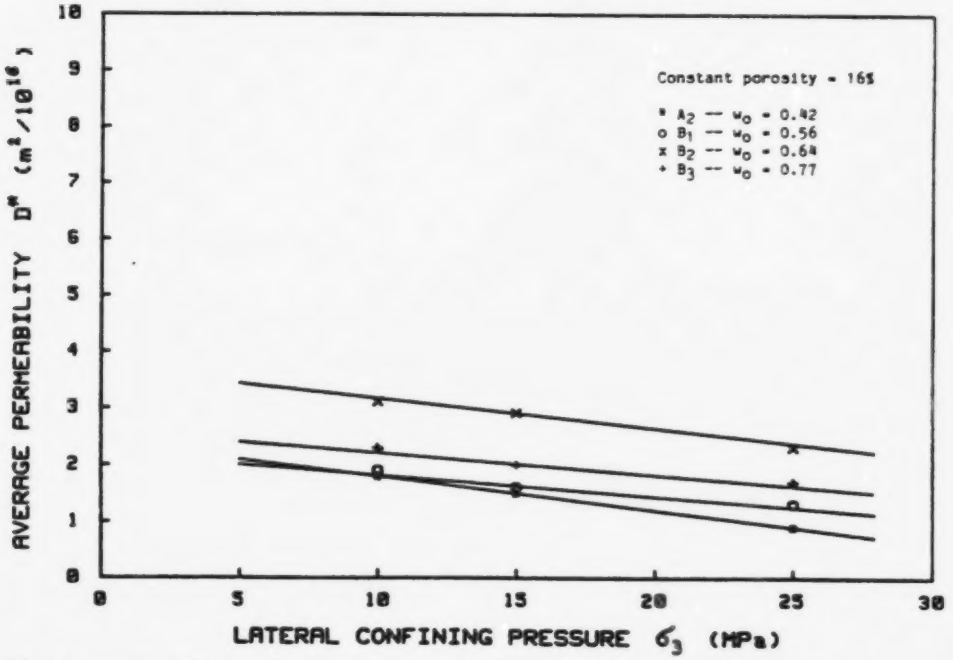

Figure 20 Linear fits of average permeability vs. lateral confining pressure σ_3, for ε_t = 16%, and variable water/cement ratio.

of D* generally decrease, with decreasing porosity ε_t and with increasing σ_3. The anomalous behaviour of the specimen with w_o = 0.42 and ε_t = 18.0 was due to excessive cracks around aggregate particles due to drying shrinkage. The linear equations relating diffusivity D* to confining pressure σ_3 are given in Table 9.

Table 9

Linear regression equations for nitrogen diffusion through concrete with 70 per cent moisture loss as influenced by lateral stress σ_3. The equations are of the form $D^* = P + Q(\sigma_3)$ with P and Q constant and r^2 = correlation coefficient.

Water/cement ratio w_o	Porosity at test (volume percent)	P $m^2/10^{16}$	Q $(m^2/MPa)/10^{16}$	r^2
0.42	18.0	7.5	-.14	0.98
0.42	16.7	2.4	-.06	1.00
0.42	11.0	0.7	-.006	0.57
0.42	10.0	3.5	-.06	0.96
0.42	16.7	2.4	-.06	1.00
0.56	15.8	2.2	-.038	0.96
0.64	15.9	3.7	-.053	0.99
0.77	15.7	2.6	-.039	0.96

5.3 Estimation of Pore Radius in Relation to Mass Transfer of Gas

When concrete takes its final set, the residual mixing water remains in an interconnected pore system. Grains of cement and aggregate assume a stable spatial configuration which is determined by a disperse system of hydration products - principally circular crystals of Ettringite - which link grains of cement but which do not fill the voids.

As hydration proceeds, the void space is partly filled by reaction products and, because the smaller spaces get filled at early ages the fine pores become progressively sealed and mass transfer of water, water vapour and gas takes place through a labyrinthine system of pores. As hydration

proceeds the new solids form partly in space separating cement grains and partly in space originally occupied by anhydrous cement. This process is illustrated in Figure 21. When terminal hydration is reached, some space

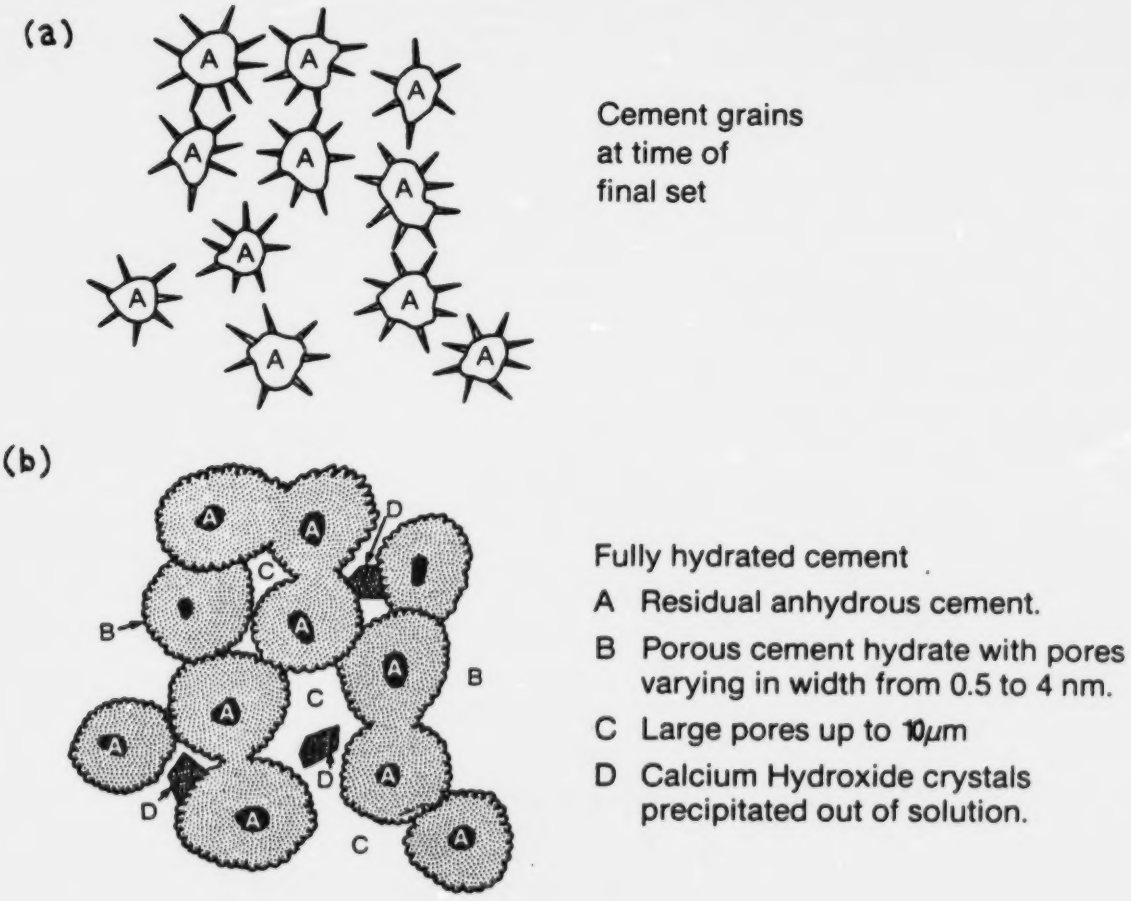
(a)
Cement grains at time of final set
(b)
Fully hydrated cement
A Residual anhydrous cement.
B Porous cement hydrate with pores varying in width from 0.5 to 4 nm.
C Large pores up to 10μm
D Calcium Hydroxide crystals precipitated out of solution.

Figure 21 Pore filling by products of hydration:
(a) Spacing of cement grains at the time of final set. Grains are fixed in position by acicular crystals, mainly Ettringite. Pores are continuous and approximately equal in volume to the initial void ratio.
(b) Fully hydrated cement paste.

between grains is completely filled with products of hydration but larger gaps are left unfilled.

Inevitably some pores are isolated while others remain connected. For perfect cement paste two types of non-solid space are recognised:

(1) Isolated pores capable of accommodating water or gas called ink-bottle pores; and

(2) Pores which are continuous throughout the concrete but which are tortuous and have varying open section.

These and other features of concrete porosity are illustrated in Figure 22.

In concrete, discontinuities at the interface between aggregate and cement paste and defects such as microcracks effectively shorten the conducting path and also provide links between ink-bottle shaped pores so that the volume fraction of the void system which is capable of mass transfer is increased.

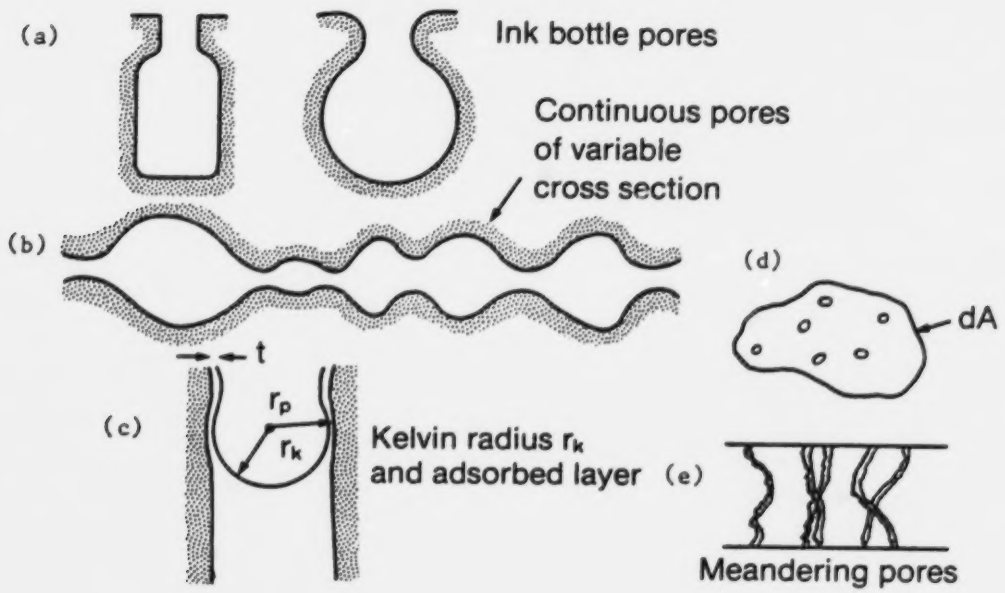

Figure 22 Model pore systems in cement paste. (a) Ink-bottle pores. (b) Continuous pores of varying cross section. (c) Pore containing condensed water and water film of thickness t on solid. (d) Pores intersecting a plane area dA. (e) Longitudinal projection of pores.

Gas transmission is complicated by the fact that condensed water acts as a barrier to mass transfer. When concrete is saturated it is effectively gas-tight. At intermediate moisture contents, the permeability to gas depends on the equilibrium vapour pressure in the pores which, in turn, determines which pores are sealed by condensed water and the thickness of water film on the walls of pores that are empty of condensed water.

5.3.1 Estimation of pore size from adsorption data

In partially saturated concrete, condensed pore water may be assumed to be in a state of uniform hydrostatic pressure so long as there is no net gain or loss of water from curved menisci. This quasi-static state may be described in terms of pore size by the Kelvin radius r_k; where

$$r_k = - \frac{2 \gamma V \cos\phi}{RT \ln(P/P_s)}; \text{ where}$$

P = the pressure in the pores of the concrete;
P_s = the saturation pressure;
γ = surface tension of condensed water (N/m);
V = molar volume of condensed water (m^3/mol);
R = the gas constant (J/°K-mol); and
T = absolute temperature (°K).
ϕ = liquid/solid contact angle usually assumed = 0°.

The thickness of the adsorbed film = t, where an approximate value is given by:

$$t = 3.5[5/\ln(P/P_s)]^{1/3}$$

and t is in metres [Ref. 12].

As a first approximation, it may be assumed that the pores are of circular cross section. Thus, at a relative vapour pressure (P/P_s) in the range permitting condensed water, all pores having a diameter $d_p \geq 2(r_K+t)$ (see Figure 22) will permit the passage of gas through an aperture having an effective diameter $d_{eff} \geq 2r_k$.

Figure 23 shows the computed sorption isotherm for A_2 concrete used in the present experiments, i.e. with $w_o = 0.42$ and $\varepsilon_1 = 23.0$ per cent together with the corresponding pore size distribution curve. In the present

project all gas transmission data was normalised at 70 per cent moisture loss. For this standard moisture loss, all pores having a diameter of 4 nm and more are capable of gas transmission. The corresponding volume of pores capable of transmitting gas is 4.6 percent of the total volume of concrete.

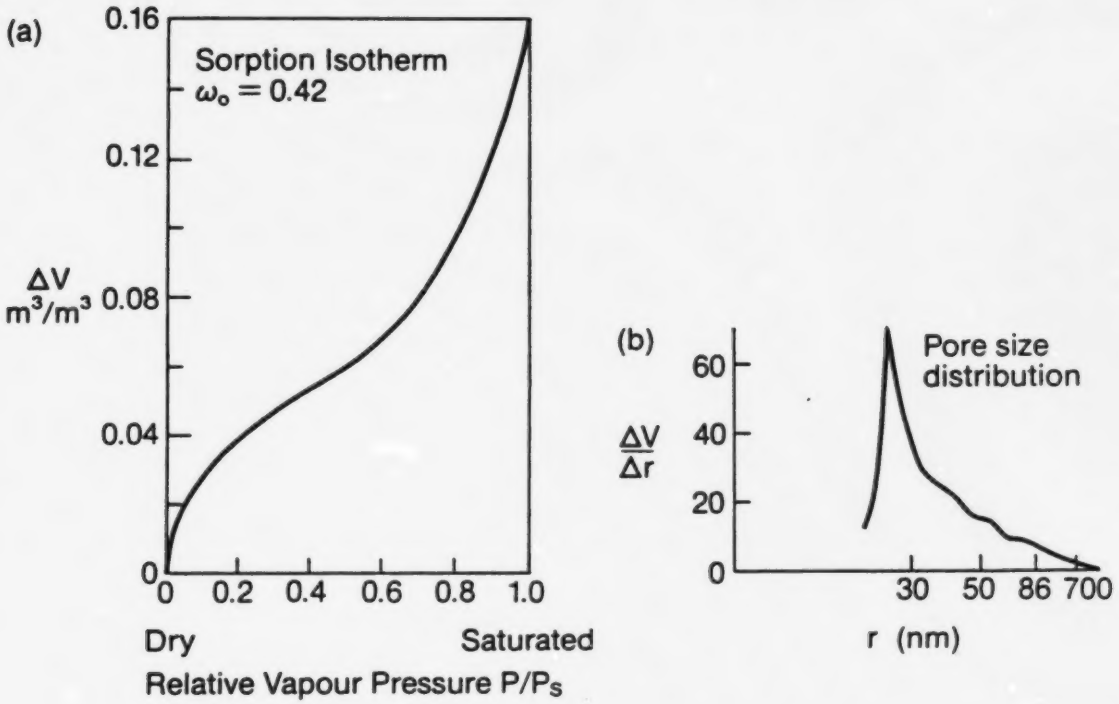

Figure 23 (a) Sorption at constant temperature = 24°C for mature A_2 concrete $w_o = 0.42$, $\varepsilon_i = 23.0$ per cent.
(b) Differential pore size distribution.

5.3.2 Estimation of hydraulic mean radius

Powers [Ref. 8] and Gregg and Sing [Ref. 12] suggested a pore size characterisation by means of a factor d/2 = the hydraulic mean radius = volume of empty pores/area of pore walls.

For the purpose of comparison we may evaluate d/2 as follows:

d/2 = (Volume of evaporable water)/(surface area of pores)
$= w_e/\Sigma_{BET}$

For the concrete of the present experiments

$$w_e = 0.287 \text{ g per gram of anhydrous cement} = 0.287 \times 10^{-6} \text{ m}^3/\text{g}$$
$$\Sigma_{BET} = 3570\ V_m\ (\text{m}^2/\text{g});$$
$$V_m = c.w_n = (0.261)(0.180) = 0.047\ \text{g/g}$$

Thus for unit mass of cement

$$d/2 = 0.287 \times 10^{-6}/(0.0470)(3570)$$
$$= 1.7 \times 10^{-9}\ \text{m}$$
$$= 1.7\ \text{nm}$$

Thus if we assume that the entire void space consists of continuous capillaries of circular cross section the hydraulic mean radius is 1.7 nm; and the corresponding pore diameter = 3.4 nm.

Table 10

Some values of the constant calculated by Gregg and Sing [Ref. 12]

Pore type	Minimium solid:solid separation distance	Hydraulic mean radius d/2
Non-intersecting cylindrical capillaries	2R	R (1)
Parallel sided fissures	2b	b
Packed spheres of diameter = 2R:		
Cubic packing--		0.613R
Rhombohedral packing--		0.229R

Note (1): This means that when the solid-solid distance is 2R, the hydraulic mean radius = R.

5.3.3 Estimation of pore size from gas flow characteristics

Huang et al [Ref 14] used nitrogen flow characteristics to estimate mean pore size. Details of the method are given in Appendix E.

Pore size estimates based on the present data are given in Table 11. It is seen that for constant porosity a* is sensibly independent of water/cement ratio but seems to vary appreciably with porosity. The effect of lateral pressure is apparently of the same order as experimental error and cannot be elucidated by these data. Values of a* are about 6 to 60 times greater than corresponding values of d/2. This is because the hydraulic mean radius calculations ignore the contribution of capillary pores to the overall porosity, and are in fact an estimate of the size of much smaller gel pores only. The mean pore radius a*, on the other hand, is based on gas flow data, and is larger than the hydraulic radius since most gas flow takes place through the larger capillary pores in the paste.

Table 11

Mean pore radius a* calculated from the data of Table 6 where a* (nm) = 635/(A/B - 2) [Ref. 13]; A and B are constants of regression lines of the form $D_n^* = A + B\,(\Delta P/P_o)$.

	Water/cement ratio w_o	Porosity ε_t%	σ_3 MPa	a* nm
Constant w_o specimens	0.42	18.0	10	11
			15	9
			25	19
	0.42	16.7	10	76
			15	84
			25	47
	0.42	11.0	10	59
			15	42
			25	64
	0.42	10.0	10	112
			15	79
			25	48

Table 11 cont'd

	Water/cement ratio w_o	Porosity ε_t%	σ_3 MPa	a* nm
Constant porosity specimens	0.42	16.7	10	76
			15	84
			25	47
	0.56	15.8	10	58
			15	111
			25	85
	0.64	15.9	10	59
			15	52
			25	42
	0.77	15.7	10	88
			15	66
			25	68

6. TESTS ON THE INFLUENCE OF REINFORCING STEEL

6.1 Specimens

Seven different reinforcing schemes as tabulated in Table 12 were used. Five specimens from each group were tested, each specimen being subjected to four or five different "runs". Dimensions of the specimens are as described in section 2.1.

Groups A, B and C had different quantities of longitudinal steel parallel to the direction of flow. Groups D and E contained two different volumes of spiral reinforcing, Group F contained the same quantity of reinforcing as Group B but it was cut into short lengths and randomly distributed in the concrete. Group G was a combination of the steel of Group B and that of Group E.

6.2 Experimental

The specimens were tested at various moisture contents between saturated and oven-dry. A second order polynomial was fitted to Moisture Loss versus Flow Rate curves, generally with a correlation coefficient of better than 0.99. From these equations, flow rates for 6 standard moisture losses

Table 12

Reinforcement Configurations Used for Gas Permeability Specimens

Group	Steel Code	Description of Reinforcing (6.35 mm)	Surface Area/Volume $10^{-3}m^{-1}$
A	2L	Two longitudinal bars	2.26
B	4L	Four longitudinal bars	4.52
C	1L	One longitudinal bar	1.13
D	S25	Spiral with 25 mm pitch	9.63
E	S50	Spiral with 50 mm pitch	5.15
F	R	50 mm randomly oriented lengths	2.26
G	4L+S50	Combined S50 and 4L	9.67
CONTROL	NIL	No reinforcement	0.00

were interpolated. These normalised values were used to calculate diffusion coefficients and characterise the performance of concrete containing the seven different configurations of reinforcement.

6.3 Results

The results are reflected in Table 13.

In each case the flow rate goes from the lowest at small moisture loss to highest in the dry state. The groups may be classified in descending order of merit as follows:

BEST	Group F	Randomly distributed steel
	C	1 Longitudinal bar
	G	Combined spiral + 4 longitudinal bar
	E	Spiral at 50 mm pitch
	B	4 Longitudinal bars
	A	2 Longitudinal bars
WORST	D	Spiral at 25 mm pitch

Table 13

Nitrogen diffusion coefficients of reinforced specimens interpolated at various moisture contents.

Specimen Group	Steel	$D^*/10^{16}$ m^2 for moisture loss per cent(1)					
		-0	-35	-45	-60	-80	-100
Control	NIL	0.00	0.020	0.025	0.035	0.120	0.35
A	2L	0.05	0.460	0.660	1.040	1.680	2.49
B	4L	0.02	0.220	0.410	0.800	1.500	2.44
C	1L	0.00	0.120	0.240	0.480	0.930	1.52
D	S25	0.05	0.05	0.23	0.67	1.55	2.76
E	S50	0.00	0.10	0.23	0.53	1.09	1.84
F	R(=4L)	0.00	0.07	0.18	0.42	0.88	1.50
G	4L+S50	0.01	0.05	0.21	0.45	0.91	1.52

(1) Note: In this table, 0 = saturated, 100 = oven-dried

The total range in the oven-dry condition for all reinforced groups is $1.50 < D^* < 2.76$ $m^2/10^{+16}$. This may be compared with values for unreinforced concrete as reported in previous sections. The values of D^* reported in the present case are between 0.07 and 1.88 times the values for oven-dried concrete and between 6.4 and 50.2 times the EMC values reported in Table 1.

Although it is clear that reinforcing steel provides a leakage path along its interface with concrete the values of D^* are extremely low and it must be concluded that undamaged concrete remains an effective barrier material, material with or without reinforcement.

7. INFLUENCE OF LATERAL PRESSURE ON WATER AND GAS PERMEANCE OF CONCRETE

Previous work [Ref. 1,15] had shown that permeability of concrete to water was profoundly influenced by lateral pre-stress. In the present investigation it was found in section 5 that the diffusion of gas was similarly influenced by lateral prestress.

Estimates of mean pore size from the rates of gas diffusion did not vary appreciably or systematically with the magnitude of lateral prestress. Recalling that mean pore size a* was calculated from:

$$a^* = (635)/(A/B - 2) \text{ where } a^* \text{ is in nm,}$$

it appears that lateral stress σ_3 reduced both the intercept A and slope B of the D_n^* versus $\Delta P/P_o$ curve. The results were not sensitive enough to support the starting hypothesis that prestress affected flow mainly by closing cracks.

8. ULTRASONIC PULSE VELOCITY (USPV) AND PERMEANCE

The speed of transmission of an ultrasonic pulse through concrete depends, inter alia, on the porosity, moisture content, presence of defects such as cracks and presence of reinforcement. USPV increases or decreases according to the square root of the ratio of dynamic elastic modulus to density. Thus if the path between emitter and receiver is intersected by voids or cracks the measured velocity decreases. If such voids or cracks become filled with water, the velocity increases.

It may be expected that USPV will decrease with increase in permeance and vice versa.

The present investigation concerns the value of USPV measurements as a non-destructive means of characterising concrete and for continuous monitoring of its effectiveness as a barrier material. For this purpose, the variation of USPV with moisture content was observed for different service conditions.

8.1 USPV and Porosity

Since elastic modulus decreases with increasing porosity it might be expected that USPV would also decrease with increased porosity.

Fig. 24 shows the results of tests on concrete with four different porosities.

The expected decrease in USPV is observed in both dry and saturated specimens but the effect is accentuated when the pores are empty.

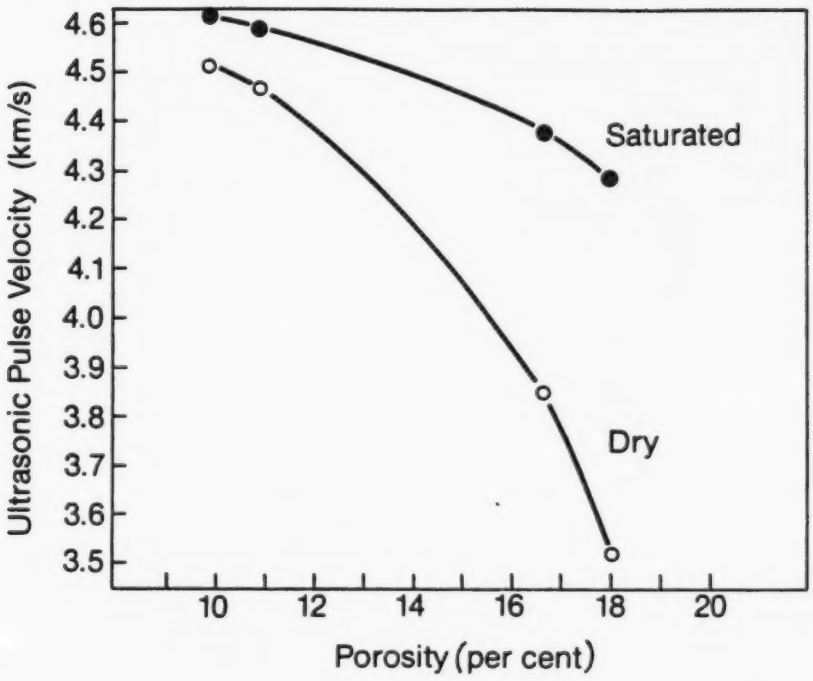

Figure 24 Variation of USPV with porosity for dry and saturated concrete.

8.2 USPV and Moisture Content

It was expected that USPV would increase with increasing moisture content and that this trend would be accentuated by severe cracking between hardened cement paste and aggregate.

The results are shown in Figure 25.

Four specimens were tested at serveral moisture contents from 0 (dry) to 100 mass percent (saturated).

It is seen that the expected relationship between moisture content and USPV is confirmed but that there is a marked difference between specimens which showed extensive cracking between matrix and interface (54 and 67) and specimens of the same mix which had few cracks (A_1 and A_2). The difference in the two groups reduced as saturation was approached.

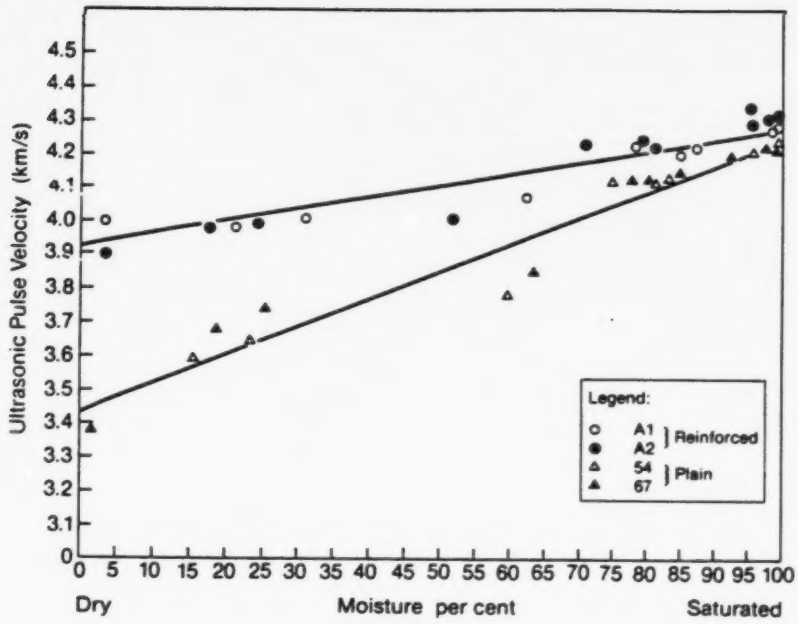

Figure 25 Variation of ultrasonic pulse velocity with moisture content for specimens previously subjected to slow drying (A_1 and A_2), and drying at 0 per cent relative humidity for 112 days (54 and 67).

8.3 USPV and Water/cement Ratio w_o

The elastic modulus of hydrated cement paste (HCP) is approximately E = 74 GPa [Ref. 3] and its density is ρ = 2.52 [Ref. 1]. These figures are sufficiently close to those of the majority of aggregates that the ratio $(E/\rho)^{1/2}$ is for practical purposes equal to that of aggregate. The water/cement ratio is only important insofar as it affects porosity.

The results of a limited test program are given in Fig. 26.

For concrete using the same cement and aggregate it was anticipated that USPV would be insensitive to w_o.

The results are scattered and it appears that there is little prospect that a relationship between USPV and w_o can be supported or disproved by these data.

8.4 USPV and Gas Permeability

Some values for coefficient of diffusivity of nitrogen D* versus USPV are given in Fig. 27 below.

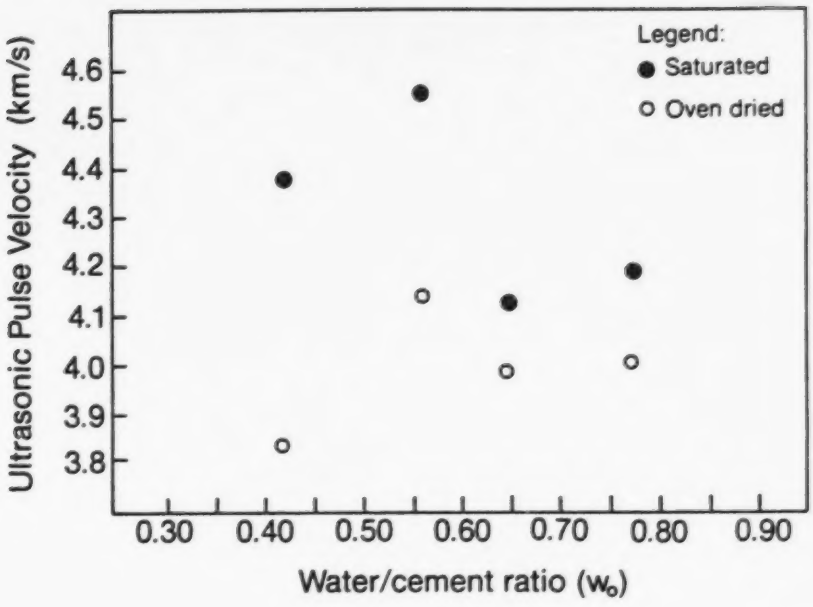

Figure 26 Variation of USPV with water/cement ratio for mixes of approximately constant porosity.

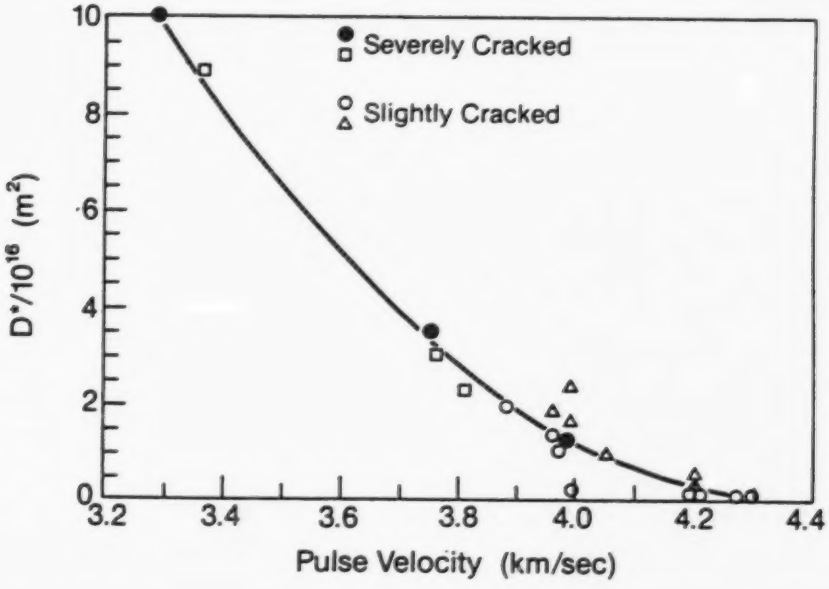

Figure 27 Relationship between coefficient of diffusivity D* and USPV for severely cracked specimens (54 and 67) and slightly cracked specimens (A_1 and A_2).

The values given in Fig. 27 were obtained at different moisture contents on specimens which had suffered various degrees of damage due to shrinkage cracking.

Figure 28 also shows a correlation between D* and USPV for six different unreinforced specimens, at their equilibrium moisture content (typically around 50% of their saturated values). Though wide, the scatter band in the D* ordinate is probably within the limits of experimental variability between different specimens of nominally identical concrete.

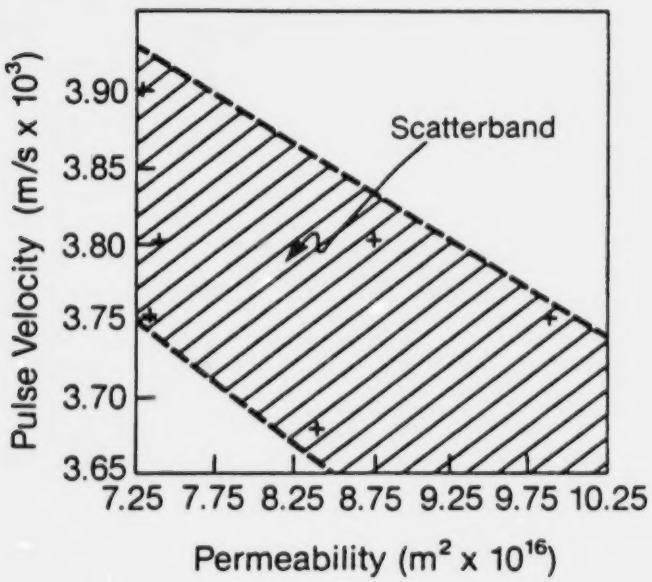

Note: generally increasing pulse velocity, with decreasing permeability.

Figure 28 Relationship between USPV and permeability for six different unreinforced specimens, as measured at the equilibrium moisture content of each specimen.

8.5 Summary

The value of ultrasonic pulse velocity for characterising concrete as a barrier material for nuclear containment structures has been demonstrated in respect of:

(1) porosity which is a basic characteristic of concrete;
(2) moisture content which, for a given porosity, determines the rate of gas transmission; and
(3) micro-cracking of the matrix due to shrinkage.

USPV is also known to be effective in detecting gross anomalies such as structural cracks and severe honeycombing of concrete and for giving a non-destructive value for concrete quality. USPV is less successful in distinguishing between (1), (2) or (3) or in determining the effects of reinforcing. The results are, however, promising enough to pursue in further testing on prototype-scale specimens.

9. INFLUENCE OF AEROSOLS ON GAS PERMEABILITIES

Vaughan [Ref. 16] quoted experiments [Ref. 17] which "indicate that deposits of particulate material play a major role in reducing the inhalation hazard following a reactor accident both by decreasing the amount of escaping particulate matter and by increasing the size of the particle agglomerates." Albrecht et al [Ref. 18] classified the structure of nuclear aerosols from molten corium-E* according to three size ranges - (a) <0.17 microns; (b) 0.17 to 0.3 microns; and (c) 0.3 to 0.73 microns.

In terms of concrete without defects it is doubtful whether there would be any penetration of such particles into the largest pores but it is conceivable that condensation might take place in cracks of, perhaps, 10 microns or more.

Some exploratory tests were made using 5 mass per cent Aluminium Chlorohydrate aerosol, and a plain water aerosol; the results are given in Table 14.

Although both aerosols exhibited some blocking effect against the diffusion of nitrogen, the effect was generally negligible, and in the case of the water aerosol, the slight reductions in permeability were likely due to the increase in the moisture content of the surface layer of concrete.

---

* The elemental composition of corium-E is: 35 mass per cent NO_2, 55 mass per cent steel and 10 mass per cent Zircaloy.

Table 14

Nitrogen permeability vs. surface treatment, for various specimens

Sample	% Moisture	Surface Treatment	Flow Rate $(m^3/s)/10^6$	Permeability $(m^2/10^{16})$
A3	30	None	3.03	2.69
		5% Aluminum Chlorohydrate Aerosol	3.00	2.66
		As above with additional water aerosol	2.63	2.30
A4	30	None	0.89	0.75
		Water aerosol	0.88	0.75
54	5*	None	9.52	9.84
		Water aerosol	8.51	8.57
56	40*	None	3.77	3.36
		Water aerosol	3.64	3.22
69	50*	None	8.00	8.16
		5 mass per cent Aluminum Chloro-hydrate Aerosol	7.70	7.67

* previously subjected to 0 per cent relative humidity for 112 days.

10. MASS TRANSFER RATES OF WATER AND GAS IN BEST AND WORST CASES

From Table C1 in Appendix C, the best and worst water permeability coefficients as determined by measuring water flow rates at known driving pressures, were $.012 \times 10^{-18}$ m^2 and 20.6×10^{-18} m^2, respectively.

From Tables 1 and 14 the best and worst nitrogen permeabilities were 0, in the case of saturated specimens, and 9.84×10^{-16} m^2 in the worst case, for a specimen which had been damaged by exposure to 0 percent relative humidity for 112 days.

Based on these permeabilities, and using Darcy's law as stated in Eqn. B4, we may calculate the actual mass transfer rates in the best and worst cases, assuming the following variables: 1000 m^2 wall area and 1 m wall thickness -- with an overpressure of 100 kPa (~1 atmosphere) within the structure.

For water:

$$\text{Best case flow rate } Q = \frac{.012\times10^{-18}\times100\times10^{3}\times1000}{910\times10^{-6}\times1}$$

$$= 1.32\times10^{-9} \text{ m}^3/\text{s}$$

$$= 0.041 \text{ m}^3/\text{year}$$

$$= 41 \text{ kg/year}$$

$$\text{Worst case flow rate } Q = \frac{20.6\times10^{-18}\times100\times10^{3}\times1000}{910\times10^{-6}\times1}$$

$$= 2.26\times10^{-6} \text{ m}^3/\text{s}$$

$$= 71 \text{ m}^3/\text{year}$$

$$= 71{,}000 \text{ kg/year}$$

For nitrogen:

Best case flow rate = 0 (if concrete were entirely saturated)

$$\text{Worst case flow rate } Q = \frac{9.84\times10^{-16}\times100\times10^{3}\times1000}{17.8\times10^{-6}\times1}$$

$$= 5.5\times10^{-3} \text{ m}^3/\text{s}$$

$$= 175{,}000 \text{ m}^3/\text{year}$$

$$= 218{,}000 \text{ kg/year}$$

In a hypothetical loss-of-coolant accident, leak rates of radioactive species may be approximated by assuming concentrations of such species in the air and water within the containment structure, and assuming that these will travel through the concrete at the same rate as the medium in which they are being carried i.e. air or water.

Prototype-scale tests will eventually serve to back up the worst case upper bound leak rates, and will presumably yield higher limits, due to the presence of inherent defects not present in the small specimens.

11. REFERENCES

1. Mills, R.H. The permeability of concrete for reactor containment vessels, INFO 0111, Atomic Energy Control Board, Ottawa, 1983.

2. Ruettgers, A., Vidal, E.N. and Wing, S.P. An investigation of the permeability of mass concrete with particular reference to Boulder Dam. J. Amer. Concrete Institute, 382-416, 1935.

3. Mather, B., Callan, E.J., McCoy, E.E. and Carlson R.W. Permeability and triaxial tests of lean mass concrete. Vicksburg US Army Waterways Experimental Station, Technical Memorandum G-380, March 1954. (see also R.E. Davies. Same title. Berkeley, US Dept. of Army, 128, April 1950).

4. Asmis, K. private communications.

5. Loughborough, M.T. Permeability of concrete to air. Ontario Hydro Research Quarterly, 14-16, 1966.

6. Darr, G.M. and Ludwig, U. Determination of permeable porosity. Materiaux et constructions, May-June 1973, No. 33, pp. 185-189.

7. Figg, J.M. Methods of measuring the air and water permeability of concrete. Magazine of Concrete Research, Vol. 25, No. 85, 213-219, Dec. 1973.

8. Powers, T.C. and Brownyard, T.L. Studies of the physical properties of Portland cement paste. J. Amer. Concrete Institute, Vol. 18, pp. 971-981, April 1947.

9. Mills, R.H. Curing of concrete at various depths from an exposed surface. Transactions of the South African Institution of Civil Engineers, Nov. and Dec. 1965.

10. Meeting at University of Toronto between K. Asmis, A. Omar and R.H. Mills at the University of Toronto.

11. Henry, R.L. and Korz, G.K. Water vapour transmission of concrete and of aggregates. U.S. Naval Civil Engineering Laboratory, Port Hueneme, California, 1963, pp. 496-498.

12. Gregg S.J. and Sing, K.S.W. Adsorption surface area and porosity, Academic Press, London, 1967, pp. 160-182.

13. Markovic, J.R. Gas transmission of concrete for nuclear containment vessels. M.A.Sc. Thesis. University of Toronto, 1985.

14. Huang, J-H., Sherwood, W.C., and Wakao, N. Determination of mean pore radii in mineral aggregates using permeability measurements. Highway Res. Board, Special report 90, Symposium on structure of Portland cement paste and concrete, pp. 219-233, Washington, 1966.

15. Mills, R.H. The influence of stress on the permeability of concrete. FIP/CPCI Symposium, Calgary, August 1984.

16. Vaughan, E.U. Simple model for the plugging of ducts by aerosol deposits. Fission Product Source Term and Transport pp. 507-508.

17. Nelson, C.T. and Johnson, R.P. Annual technical progress report. LMFBR Safety program, GFY 1977 A1-DOI-13210 (Dec. 1977).

18. Albrecht, A., Matschoss, V. and Wild, H. Release of fission and activation products during LWR core meltdown. ENS/ANS International Topical Meeting on Nuclear Power Reactor Safety. Brussels, October 1978, pp. 2304-2314.

19. Mills, R.H. Factors influencing cessation of hydration in water cured cement pastes. Structures of Portland Cement Paste and Concrete SR 90, Highway Res. Board, pp. 406-424.

20. Powers, T.C. The Physical Structure of Portland Cement Paste, in Taylor , H.F.W. The Chemistry of Cements, V. 1, Academic Press, London, 1964, p. 402.

APPENDIX A

Volume Distribution of Phases in Concrete

The entire quality spectrum of structural concrete is determined by mixing water W between 120 and 240 kgm^{-3} and water/cement ratio, w_o between 0.28 and 0.75. Taking the density of anhydrous Portland cement = 3220 kgm^{-3}, we obtain extreme values of cement paste content as follows.

		Mass kgm^{-3}		Volume lm^{-3}			
Strength (MPa)	w_o	W	C	Water	Cement	Paste	Aggregate
90	0.28	250	857	240	266	506	494
20	0.75	120	160	120	50	170	830

In practice, for concrete in the strength range 30 to 50 MPa, w_o varies between 0.45 and 0.6 and W varies between 160 and 200 kgm^{-3}; the aggregate volume varies between 660 and 770 lm^{-3}, the paste content between 340 and 230 litres/cubic metre and initial porosity between 0.16 and 0.20.

When water reacts chemically with unit mass of Portland cement the amount of combined water is $w_n^o = 0.253$ and its volume is that of unit mass of Portland cement, plus 0.2530 mass of water, minus chemical shrinkage. The chemical shrinkage has been found to be V = 0.2584 x the volume of chemically combined water.

We may compute for completely hydrated cement:

For arbitrary volume		For 1 m^3 of hydrate	
Mass	Volume	Mass (kg)	Volume (l)
1.000	0.3106	2007	623
0.253	0.1876	508	377
1.253	0.4982	2515	1000

In nature, cement is never completely hydrated and the ultimate degree of hydration may be determined [Ref. 19] by the empirical relationship

$$\alpha^* = \frac{1.031\ w_o}{0.194 + w_o} \qquad \text{(A1)}$$

Thus, at ultimate hydration we compute

(a) For unit mass cement	Arbitrary Units Mass	Volume
Unhydrated cement	$1-\alpha^*$	$\frac{1}{3.22}(1-\alpha^*)$
Hydrated cement	$1.253\alpha^*$	$\frac{1}{2.515}(1.253\alpha^*)$
Evaporable water	$w_o - 0.1876\alpha^*$	$w_o - 0.1876\alpha^*$
TOTALS	$1 + w_o + 0.0654\alpha^*$	$\frac{1}{3.22} + w_o$

(b) For $1m^3$ of cement paste	Mass (kg)	Volume (ℓ)
Unhydrated cement	$\frac{3220(1-\alpha^*)}{1 + 3.22\ w_o}$	$\frac{1000(1-\alpha^*)}{1 + 3.22w_o}$
Hydrated cement	$\frac{4035\alpha^*}{1 + 3.22w_o}$	$\frac{1604\alpha^*}{1 + 3.22w_o}$
Evaporable water	$\frac{3220w_o - 604\alpha^*}{1 + 3.22w_o}$	$\frac{3220w_o - 604\alpha^*}{1 + 3.22w_o}$
TOTALS	$\frac{3220(1+w_o) + 211\alpha^*}{1 + 3.22w_o}$	1000

Considering now 1 m^3 of paste and following Powers [Ref. 20] we assume the surface area of hydrated cement = 210 m^2g^{-1} and therefore, for one cubic metre:

$$\text{Surface area} = \frac{210{,}000 \times 4035\alpha^*}{1 + 3.22w_o}$$

$$= \frac{847 \times 10^6\alpha^*}{1 + 3.22w_o}\ m^{-1}\ m^2/m^3 \qquad \text{(A2)}$$

The volume of evaporable water (i.e. the pore volume, by definition) =

$$\frac{3.22\ w_o\ - .604\ \alpha^*}{1 + 3.22\ w_o}\ m^3/m^3$$

Therefore based on hydration parameters only, an estimate of the hydraulic mean radius is given by

$$d/2 = \frac{w_e}{\Sigma_{BET}} = \frac{3.22\ w_o - .604\ \alpha^*}{1 + 3.22\ w_o} \times \frac{1 + 3.22\ w_o}{847 \times 10^6\ \alpha^*}$$

$$= \frac{3.22\ w_o - .604\ \alpha^*}{847 \times 10^6\ \alpha^*}\ m \qquad \text{(A3)}$$

Using Eqn. A3, values of hydraulic mean radius can be calculated which are comparable to those calculated in section 5.3.2.

APPENDIX B

Commentary on the Significance and Derivation of the Permeability Coefficients, k and D*

The permeability coefficients k and D* both derive from the same source, namely, Darcy's law. Darcy's law is perhaps the most fundamental relationship in the physics of flow through porous media, and relates the volume flow rate of a fluid passing through a porous medium, to the imposed pressure gradient across the medium. One way of writing Darcy's law is as follows:

$$Q = \frac{kA\Delta h}{\ell} \qquad (B1)$$

where Q = steady state volume flow rate, measured at outlet pressure (m^3/s)
A = constant cross-sectional area of the medium (m^2)
Δh = pressure head of the fluid (m)
ℓ = "thickness" of the medium, or the shortest path length which the fluid must traverse in order to pass through the medium
k = a constant

Thus, Darcy's law states that the rate of flow of the fluid through the porous medium is directly proportional to the pressure gradient causing the flow. Fig. B1 illustrates the significance of the parameters in Darcy's law, as well as schematically representing the basic experimental method.

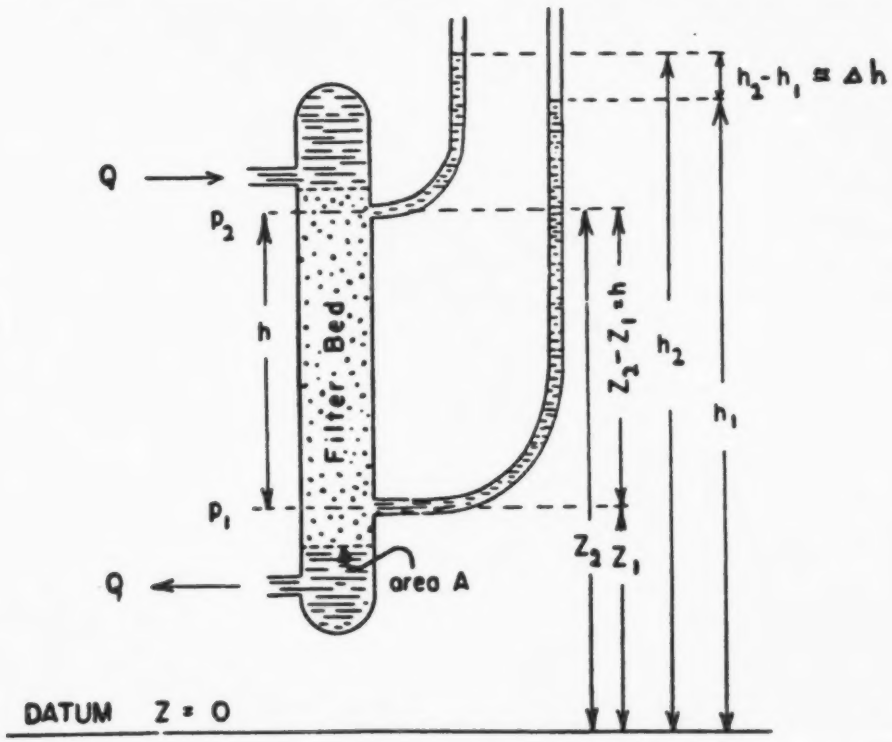

Figure B1 Darcy's filtration experiment[1]

As Darcy's law stands in eq. B1, the constant k may be thought of as the velocity of the percolating fluid per unit drop of hydraulic head. The validity of Darcy's law has been tested and shown to be true for a wide variety of experimental conditions, though it has been shown to be invalid for liquids at high velocities, and for gases at very low and at very high velocities through the medium.

Although the constant k is sometimes mistakenly referred to as "the permeability" of a medium, on closer inspection it in fact represents a combination of properties of both the porous medium and the fluid. If one is only performing comparative permeability studies, as was done earlier in this report, then it is quite acceptable to use only one fluid (e.g. water) to arrive at k values for a number of different mediums, in order to test for differences in permeability among samples. This is what was described in section 4, where water permeability tests were used as a basis for comparison among several different concrete specimens.

However, it is possible to obtain a more fundamental permeability coefficient, which is dependent only on the properties of the medium, and not the fluid, by introducing the dynamic fluid viscosity into Darcy's equation.

First, the height differential, Δh (equal to h_2-h_1, in Fig. B1), representing the pressure drop across the medium, can be converted into a pressure differential ΔP, so that

$$Q = k'A \cdot \frac{\Delta P}{\ell} \qquad \text{(B2)}$$

where $k' = k/\rho g$, ρ is the density of the fluid, and ΔP is the pressure differential across the medium, measured in suitable units (e.g. MPa).

We can now isolate the effect of the fluid by introducing a new constant, $D^* = k'\mu$ (or $k' = D^*/\mu$) where μ is the fluid viscosity and D^* is the "specific permeability" of the medium, in units of m^2. The specific permeability (sometimes written as D_s or D_s^*) is a fundamental constant of the porous medium, and not dependent on the properties of the fluid. Hence Darcy's law can also be presented as

$$Q = \frac{D^*}{\mu} \cdot \frac{A\Delta P}{\ell} \qquad \text{(B3)}$$

from which we get

$$D^* = \frac{\mu \cdot \ell \cdot Q}{\Delta P \cdot A} \qquad \text{(B4)}$$

The water permeability figures presented in section 4 as "k" values, were derived from the first form of Darcy's law (eq. B1), whereas the gas permeabilities in section 5, presented as "D*" values, were derived from the second form of Darcy's law (eq. B4). So although it appears that we are dealing with two different permeabilities, we are dealing with only one but presenting them in alternative forms.

For comparative studies of various porous mediums, it is sufficient to use the first form of Darcy's law to determine "k" values; but if it is desired to find more fundamental relationships (e.g. permeability vs. porosity or permeability vs. moisture content, etc.) it is necessary to use the form of Darcy's law which takes into account the fluid viscosity, so that D* values may be calculated.

---

[1] Scheidegger, A.E., The physics of flow through porous media, University of Toronto Press, 1957, p.56.

APPENDIX C

Measured Water Flow Rate dQ/dt (m^3/s) as Influenced by Confining Pressure σ_3 and Pressure Gradient $\Delta h/\ell$.

Table C1

Specimens in this group had constant water/cement ratio and various porosities. (Specimen identification includes: mix references $A_1, A_2 \cdots$, $B_2, B_3, \ldots$; w_o = water/cement ratio, ε_i = initial void ratio, ε_t = void ratio at the time of test.)

Specimen identification	σ_3 [MPa]	$\frac{\Delta h}{\ell}$	$\frac{dQ}{dt}[\frac{m^3}{sec}]$ /10^{12}	$k[\frac{m}{s}]$ /10^{12}	D* $[m^2]/10^{18}$
A1	5	1460	742	222(1)	20.6(2)
	5	2435	725	130	12.1
w_o=0.42	5	5269	704	58	5.4
ε_i=29.2%	10	1615	438	119	11.1
ε_t=18.0%	10	2712	630	102	9.5
	10	5058	987	85	7.9
	15	1346	215	70	6.5
	15	2712	443	71	6.6
	15	5269	744	62	5.8
A2	5	1462	191	58	5.4
	5	2903	245	37	3.4
w_o=0.42	5	5577	471	38	3.5
ε_i=23.0%	10	1711	184	48	4.5
ε_t=16.7%	10	2827	126	20	1.9
	10	5480	320	26	2.4
	15	1750	86	22	2.0
	15	3173	80	11	1.0
	15	5423	179	15	1.4

Specimen identification	σ_3 [MPa]	$\frac{\Delta h}{L}$	$\frac{dQ}{dt}[\frac{m^3}{sec}]$ /10^{12}	$k[\frac{m}{s}]$ /10^{12}	D* [m^2]/10^{18}
A3	5	1919	1.5	0.35	.032
	5	2923	2.4	0.36	.033
w_o=0.42	5	5403	1.8	0.15	.014
ε_i=17.6%	10	1846	1.6	0.38	.035
ε_t=11.0%	10	2808	1.2	0.19	.018
	10	5558	1.6	0.13	.012
	15	1327	0.7	0.23	.021
	15	2712	0.7	0.05	.005
	15	5404	0.8	0.07	.007
A4	5	1846	12.3	2.9	.270
	5	3019	18.2	2.6	.240
w_o=0.42	5	5173	13.3	1.1	.102
ε_i=15.0%	10	2115	5.0	1.0	.093
ε_t=10.0%	10	2711	6.9	1.1	.102
	10	5346	2.2	0.17	.016
	15	1962	4.7	1.0	.093
	15	2046	3.3	0.50	.046
	15	5481	2.6	0.21	.019

(1) This means 222×10^{-12} m/s

(2) This means 20.6×10^{-18} m^2

Note that: $D^* = \frac{k\mu}{\rho g} = \frac{k(0.91\times10^{-6})}{1000(9.8)}$ (for water permeant)

$= 9.28\times10^{-8}$ (k) (see Appendix B for a derivation)

Table C2

Measured flow rate dQ/dt for different confining pressures σ_3 and pressure gradients $\Delta h/\ell$ for specimens with constant initial porosity ε_i and various water/cement ratios w_o.

Specimen	σ_3 [MPa]	$\frac{\Delta h}{\ell}$	$\frac{dQ}{dt}[\frac{m^3}{sec}]$ /10^{12}	$K[\frac{m}{s}]$ /10^{12}	D* [m2]/10^{18}
A2	5	1462	191	58	5.4
	5	2903	245	37	3.4
w_o=0.42	5	5577	471	38	3.5
ε_i=23.0%	10	1711	184	48	4.4
ε_t=16.7%	10	2827	126	10	0.9
	10	5480	320	26	2.4
	15	1750	86	22	2.0
	15	3173	80	11	1.0
	15	5423	179	15	1.4
B1	5	1919	394	91	8.4
	5	2538	595	105	9.8
w_o=0.56	5	5404	524	43	4.0
ε_i=23.0%	10	1289	81	28	2.6
ε_t=15.8%	10	2673	231	38	3.5
	10	5346	436	36	3.3
	15	1346	32	11	1.0
	15	2712	77	13	1.2
	15	5348	212	18	1.7
B2	5	1346	14	5	0.5
	5	2846	21	3	0.3
w_o=0.64	5	5423	63	5	0.5
ε_i=23.0%	10	1288	20	7	0.7
ε_t=15.9%	10	2577	21	4	0.4
	10	4731	54	5	0.5
	15	1346	16	6	0.6
	15	2846	63	10	0.9
	15	5077	50	4	0.4

Specimen	σ_3 [MPa]	$\frac{\Delta h}{L}$	$\frac{dQ}{dt}[\frac{m^3}{sec}]$ /10^{12}	$K[\frac{m}{s}]$ /10^{12}	D* $[m^2]/10^{18}$)
B3	5	1712	19	5	0.5
	5	2846	33	5	0.5
w_o=0.77	5	5384	62	5	0.5
ε_i=23.0%	10	2308	15	3	0.3
ε_t=15.7%	10	3096	24	3	0.3
	10	5288	44	4	0.4
	15	2077	7	1	0.1
	15	2923	16	2	0.2
	15	5481	37	3	0.3

APPENDIX D

Variation of diffusion coefficient D* with confining pressure and upstream pressure for values of dQ/dt interpolated at 70 per cent moisture loss. Included are normalized values of D*, which when plotted against normalized pressures $\Delta P/P_o$, yield linear regression constants which can be used in mean pore diameter calculations.

Table D1

(a) ε_i = 29.2 and ε_t = 18.0 volume per cent, w_o = 0.42.

Specimen	σ_3 MPa	ΔP MPa	dQ/dt $(m^3/s)/10^6$	D* $m^2/10^{16}$	D_n^* (1) $(m^2/s)/10^6$
A_1	10	.689	0.62	3.6	2.0
		1.379	1.83	5.4	3.1
		2.758	5.81	8.5	4.8
		5.516	10.11	7.4	4.2
	15	.689	0.52	3.1	1.8
		1.379	1.59	4.7	2.7
		2.758	4.53	6.6	3.8
		5.516	8.51	6.2	3.5
	25	.689	0.37	2.2	1.3
		1.379	1.14	3.3	1.9
		2.758	3.28	4.8	2.7
		5.516	7.70	5.6	3.2

(1) $D_n^* = D^*/(\mu/P_o)$ where $\mu = 1.78 \times 10^{-5}$ N.s/m^2 (viscosity of nitrogen) and P_o = .1013 MPa. Alternately, $D_n^* = \dfrac{Q.\ell}{A(\Delta P/P_o)}$

Table D1 (cont'd)

(b) ε_i = 23.0 and ε_t = 16.7 volume per cent, w_o = 0.42.

Specimen	σ_3 MPa	ΔP MPa	dQ/dt $(m^3/s)/10^6$	D^* $m^2/10^{16}$	$D_n^*(m^2/s)/10^6$
A_2	10	.689	0.14	0.8	0.5
		1.379	0.40	1.2	0.7
		2.758	1.25	1.9	1.1
		5.516	4.44	3.3	1.9
	15	.689	0.12	0.7	0.4
		1.379	0.33	1.0	0.6
		2.758	1.03	1.5	0.9
		5.516	3.80	2.8	1.6
	25	.689	0.08	0.5	0.29
		1.329	0.20	0.6	0.35
		2.758	0.70	1.0	0.6
		5.516	2.10	1.6	0.9

(c) ε_i = 17.6 and ε_t = 11.0 volume per cent, w_o = 0.42.

Specimen	σ_3 MPa	ΔP MPa	dQ/dt $(m^3/s)/10^6$	D^* $m^2/10^{16}$	$D_n^*(m^2/s)/10^6$
A_3	10	.689	0.06	0.3	0.17
		1.379	0.18	0.5	0.29
		2.758	0.52	0.8	0.5
		5.516	1.70	1.2	0.7
	15	.689	0.06	0.3	0.17
		1.379	0.16	0.5	0.29
		2.758	0.48	0.7	0.4
		5.516	1.56	1.1	0.6
	25	.689	0.05	0.3	0.17
		1.379	0.14	0.4	0.23
		2.758	0.42	0.6	0.35
		5.516	1.39	1.0	0.6

Table D1 (cont'd)

(d) ε_i = 15.0 and ε_t = 10.0 volume per cent, w_o = 0.42.

Specimen	σ_3 MPa	ΔP MPa	dQ/dt $(m^3/s)/10^6$	D^* $m^2/10^{16}$	$D_n^*(m^2/s)/10^6$
A_4	10	.689	0.21	1.2	0.7
		1.379	0.66	1.9	1.1
		2.758	2.09	3.0	1.7
		5.516	7.73	5.5	3.1
	15	.689	0.20	1.1	0.6
		1.379	0.63	1.8	1.0
		2.758	1.75	2.5	1.4
		5.516	6.19	4.4	2.5
	25	.689	0.18	1.0	0.6
		1.379	0.50	1.4	0.8
		2.758	1.41	2.0	1.1
		5.516	4.68	3.4	1.9

(e) ε_i = 23.0 and ε_t = 15.8 volume per cent, w_o = 0.56.

Specimen	σ_3 MPa	ΔP MPa	dQ/dt $(m^3/s)/10^6$	D^* $m^2/10^{16}$	$D_n^*(m^2/s)/10^6$
B_1	10	.689	0.16	1.0	0.6
		1.379	0.42	1.2	0.7
		2.758	1.25	1.9	1.1
		5.516	4.44	3.3	1.9
	15	.689	0.12	0.7	0.4
		1.379	0.35	1.0	0.6
		2.759	1.09	1.6	0.9
		5.516	4.05	3.0	1.7
	25	.689	0.09	0.5	0.29
		1.379	0.29	0.9	0.5
		2.758	0.92	1.4	0.8
		5.516	3.08	2.3	1.3

Table D1 (cont'd)

(f) ε_i = 23.0 and ε_t = 15.9 volume per cent, w_o = 0.64.

Specimen	σ_3 MPa	ΔP MPa	dQ/dt $(m^3/s)/10^6$	D^* $m^2/10^{16}$	D_n^* $(m^2/s)/10^6$
B_2	10	.689	0.25	1.5	0.85
		1.379	0.64	1.9	1.1
		2.758	2.45	3.7	2.1
		5.516	7.01	5.3	3.0
	15	.689	0.25	1.5	0.85
		1.379	0.64	1.9	1.1
		2.758	2.12	3.2	1.8
		5.516	6.61	5.0	2.8
	25	.689	0.23	1.4	0.8
		1.379	0.49	1.5	0.85
		2.758	1.56	2.4	1.4
		5.516	5.05	3.8	2.2

(g) ε_i = 23.0 and ε_t = 15.7 volume per cent, w_o = 0.77.

Specimen	σ_3 MPa	ΔP MPa	dQ/dt $(m^3/s)/10^6$	D^* $m^2/10^{16}$	D_n^* $(m^2/s)/10^6$
B_3	10	.689	0.21	1.2	0.7
		1.379	0.51	1.5	0.85
		2.758	1.55	2.3	1.3
		5.516	5.84	4.4	2.5
	15	.689	0.16	1.0	0.57
		1.379	0.45	1.3	0.74
		2.758	1.41	2.1	1.2
		5.516	4.78	3.6	2.0
	25	.689	0.14	0.8	0.45
		1.379	0.39	1.2	0.7
		2.758	1.16	1.7	0.9
		5.516	3.87	2.9	1.7

APPENDIX E

A Derivation of the Permeability Flow Measurement Method for Calculating Mean Pore Radius a*.[1]

The flow rate of a gas through a capillary of radius a cm is expressed in moles per sec as

$$N = -(\pi a^2)\left(\frac{C}{RT}\right)\frac{dp}{dx} \tag{E1}$$

where
R is the gas constant, dyne-cm/g-mole (deg K),
T is the temperature in deg K, and

$\frac{dp}{dx}$ is the pressure gradient in dyne/cm^3.

$$C = D_{KA}\,\frac{1 + \left(\frac{\pi}{4}\right)\left(\frac{2a}{\lambda}\right)}{1 + \left(\frac{2a}{\lambda}\right)} + \frac{\frac{a^2 p}{8\mu}}{1 + \left(\frac{\lambda}{2a}\right)} \tag{E2}$$

where λ represents the mean free path in cm and μ is viscosity in g/cm/sec; D_{KA} is Knudsen diffusivity in cm^2/sec:

$$D_{KA} = \frac{2\bar{v}a}{3} \tag{E3}$$

Eq. E2 shows that C reduces to $a^2p/8\mu$ (the Poiseuille flow) as capillary radius becomes large, and that the first term (diffusion and slip flow) tends to be dominant as capillary radius and/or the pressure decreases.

For flow through porous media, Eq. E1 is modified as follows:

$$N = -f\left(\frac{AC}{RT}\right)\frac{dp}{dx} \tag{E4}$$

where f represents the area fraction effective for fluid flow. Comparison of Darcy's law, Eq. B4, with Eq. E4 indicates that

$$D^* = \frac{C\mu}{p} \cdot f \tag{E5}$$

According to the kinetic theory of gases the viscosity μ is independent of pressure and the mean free path is inversely proportional to the pressure,

$$\lambda p = \lambda_o p_o \tag{E6}$$

where λ_o is the mean free path at the reference pressure p_o. In the subsequent treatment, the reference pressure is taken as one atmosphere.

When mean pore radius $\bar{a}$ is substituted for a in Eq. E2 and Eq. E2 is substituted into Eq. E4, integration between p_1 at $x = 0$ and p_2 at $x = L$ yields

$$\frac{NRT}{p_o} = \frac{fA}{L}\left[\left[\frac{\left(1 - \frac{\pi}{4}\right)\bar{D}_{KA}}{\frac{2\bar{a}}{\lambda_o}} + \frac{\bar{a}^2 p_o}{8\mu\left(\frac{2\bar{a}}{\lambda_o}\right)^2}\right] \ln\left[\frac{1 + \left(\frac{2\bar{a}}{\lambda_o}\right)\left(\frac{p_1}{p_o}\right)}{1 + \left(\frac{2\bar{a}}{\lambda_o}\right)\left(\frac{p_2}{p_o}\right)}\right]\right.$$

$$\left. + \left[\frac{\pi\bar{D}_{KA}}{4p_o} + \frac{\bar{a}^2\left[\left(\frac{2\bar{a}}{\lambda_o}\right)\left(\frac{p}{p_o}\right) - 1\right]}{8\mu\left(\frac{2\bar{a}}{\lambda_o}\right)}\right]\Delta p\right] \tag{E7}$$

Gas kinetics indicate that Knudsen diffusivity is expressed as

$$\bar{D}_{KA} = \frac{2\bar{v}\bar{a}}{3}$$

viscosity μ as

$$\mu = \frac{pM\bar{v}}{2RT}\lambda \tag{E8}$$

where M is the molecular weight, g/g-mole, and the mean molecular velocity $\bar{v}$ is

$$\bar{v} = \sqrt{\frac{8RT}{\pi M}} \tag{E9}$$

Using Eqs. E8 and E9, Eq. E7 is rewritten as

$$Q_o = \frac{NRT}{p_o} = \frac{fA}{L}\Big\{ 0.2882\, D_{AA_o} \ln\left[\frac{1 + \left(\frac{2\bar{a}}{\lambda}\right)\left(\frac{p_1}{p}\right)_o}{1 + \left(\frac{2\bar{a}}{\lambda_o}\right)\left(\frac{p_2}{p_o}\right)}\right]$$

$$+ \bar{D}_{KA}\left[0.7118 + (0.0736)\left(\frac{2\bar{a}}{\lambda_o}\right)\left(\frac{p_2}{p_o}\right)\right]\frac{\Delta p}{p_o} + \bar{D}_{KA}(0.0368)\left(\frac{2\bar{a}}{\lambda_o}\right)\left(\frac{\Delta p}{p_o}\right)^2\Big\} \qquad \text{(E10)}$$

where Q_o is the volumetric flow rate at the reference pressure, p_o, and D_{AA_o} is the molecular diffusivity at the reference pressure

$$D_{AA_o} = \frac{\bar{v}\lambda_o}{3} \qquad \text{(E11)}$$

It is obvious that, in most cases, the first term is negligible compared with the last two terms. With this approximation, Eq. E10 is simplified as

$$\frac{Q_o L}{A\left(\frac{\Delta p}{p_o}\right)} = \alpha + \beta\left(\frac{\Delta p}{p_o}\right) \qquad \text{(E12)}$$

where

$$\alpha = f\bar{D}_{KA}\left[0.7118 + (0.0736)\left(\frac{2\bar{a}}{\lambda_o}\right)\left(\frac{p_2}{p_o}\right)\right]$$

$$\beta = f\bar{D}_{KA}\,(0.0368)\left(\frac{2\bar{a}}{\lambda_o}\right) \qquad \text{(E13)}$$

When the flow rates are plotted as $Q_oL/A\ (\Delta p/p_o)$ vs $(\Delta p/p_o)$, straight lines will be drawn. The ratio of intercept α to slope β enables the calculation of the mean pore radius $\bar{a}$ as

$$\frac{\alpha}{\beta} = 2\left(\frac{p_2}{p_o}\right) + \frac{0.7118}{0.0368\left(\frac{2\bar{a}}{\lambda_o}\right)} \qquad \text{(E14)}$$

Thus, from the values of both $\bar{a}$, and either α or β the effective area f is determined.

Substituting $p_2 = p_o = 1$ atmosphere and, $\lambda_o = 0.0657 \times 10^{-4}$ cm, (the mean free path of nitrogen at 24°C and 1 atmosphere), Eqs. E13 and E14 reduce to

$$\beta = 3.54 \times 10^{8} f \bar{a}^2 \qquad \text{(E15)}$$

$$\frac{\alpha}{\beta} = 2 + \frac{0.635 \times 10^{-4}}{\bar{a}} \qquad \text{(E16)}$$

where $\bar{a}$ is mean pore radius in cm.

---

[1] Huang, J-H., Sherwood, W.C., and Wakao, N. Determination of mean pore radii in mineral aggregates using permeability measurements. Highway Res. Board Special report 90, Symposium on structure of Portland cement paste and concrete, pp. 219-233, Washington, 1966.